

IMPERIAL

**Reconfigurable Intelligent Surfaces:
Beamforming, Modulation, and Channel Shaping**

Yang Zhao

Supervisor: Prof. Bruno Clerckx

Department of Electrical and Electronic Engineering
Imperial College London

This dissertation is submitted for the degree of
Doctor of Philosophy

Declaration

The contents presented in this dissertation are original and have been carried out by myself under the guidance of my supervisor Prof. Bruno Clerckx. Any work from other researchers, scholars, or sources have been properly cited and acknowledged. Figures, tables, and results presented in this dissertation are generated by myself, unless otherwise stated. I would like to acknowledge the use of large language models for assistance in improving the clarity and readability of introduction and background sections of this thesis. The contents have not been submitted in whole or in part for consideration of any other degree or qualification in any academic institution. I am aware of the ethical standards and academic integrity policies of Imperial College London, and I have adhered to these principles throughout the course of study. In signing this declaration, I affirm my commitment to academic honesty, intellectual integrity, and the pursuit of knowledge in the service of truth and understanding.

The copyright of this thesis rests with the author. Unless otherwise indicated, its contents are licensed under a Creative Commons Attribution-Non Commercial 4.0 International License (CC BY-NC). Under this license, you may copy and redistribute the material in any medium or format. You may also create and distribute modified versions of the work. This is on the condition that: you credit the author and do not use it, or any derivative works, for a commercial purpose. When reusing or sharing this work, ensure you make the license terms clear to others by naming the license and linking to the license text. Where a work has been adapted, you should indicate that the work has been changed and describe those changes. Please seek permission from the copyright holder for uses of this work that are not included in this license or permitted under UK Copyright Law.

Any comments, suggestions, or corrections are greatly acknowledged and can be sent to i@snowztail.com. The source code of all simulation results in this dissertation are publicly available at <https://github.com/snowztail/>. Finally, I would like to appreciate Bruno, my colleagues, and whoever is reading this dissertation.

Yang Zhao
March 2024

Abstract

Reconfigurable Intelligent Surface (RIS) is the most promising physical-layer technology for 6G. It adopts many low-power scattering elements to customize the propagation environment for improved network performance, unlocking a new potential of *channel design* as never before. In this dissertation, we first provide an overview of its structure, characteristics, applications, principles, and models, then discuss how it addresses the key issues in Simultaneous Wireless Information and Power Transfer (SWIPT) and compare it with Backscatter Communication (BackCom) in terms of functionalities, principles, models, and preferences. The work chapters investigate three typical use cases of RIS: Joint design with transceiver for a particular objective (beamforming); ride its own information over legacy networks (modulation); and manipulate the wireless environment as a stand-alone device (channel shaping). In particular, we address the following topics:

- *RIS-aided SWIPT*: We introduce RIS into multi-antenna, multi-carrier SWIPT systems, investigating joint waveform and beamforming design for maximizing harvested energy under various communication rate constraints. Algorithms, performance trade-offs, and asymptotic behaviors are analyzed.
- *RIScatter*: This novel scatter protocol integrates RIS and BackCom from an input distribution perspective. The reflection pattern is exploited simultaneously for primary-link beamforming and backscatter-link modulation. We propose a practical cooperative receiver, characterize the achievable rate region, and analyze the impact of system parameters.
- *Multiple-Input Multiple-Output (MIMO) channel shaping*: We exploit an advanced Beyond-Diagonal (BD)-RIS architecture for singular value redistribution and power maximization in Point-to-point Channel (PC), and leakage interference minimization in Interference Channel (IC). Their implications on rate-optimal joint designs are also discussed. We highlight the unique features of BD-RIS and propose an efficient design framework.

Table of contents

List of figures	xi
List of tables	xiii
Abbreviations	xv
Notation	xix
1 Introduction	1
1.1 Motivation	1
1.2 Overview on Reconfigurable Intelligent Surface (RIS)	3
1.2.1 Concept	3
1.2.2 Characteristics	3
1.2.3 Applications	5
1.3 Outline and Contributions	5
1.4 Publications	7
2 Background	9
2.1 Reconfigurable Intelligent Surface (RIS)	9
2.1.1 Programmable Metamaterials	9
2.1.2 Wave Scattering Models	12
2.1.2.1 Principles	12
2.1.2.2 Diagonal Phase Shift Model	13
2.1.2.3 Beyond-Diagonal (BD) Model	13
2.2 Wireless Power Transfer (WPT)	16
2.2.1 Introduction	16
2.2.2 Modules and Coupling Effect	18
2.2.3 Non-Linear Harvester Behavior	19
2.2.3.1 Equivalent Circuits	19

2.2.3.2	Operation Regions and Signal Models	20
2.3	Simultaneous Wireless Information and Power Transfer (SWIPT)	22
2.3.1	Introduction	22
2.3.2	Rate-Energy (R-E) Tradeoff	23
2.3.3	Modules and Operation Modes	23
2.3.3.1	Information and Energy Flows	23
2.3.3.2	Receiver Architectures	24
2.4	Backscatter Communication (BackCom)	26
2.4.1	Introduction	26
2.4.2	Modulation and Coding Schemes	27
2.4.3	Applications	29
2.4.3.1	Monostatic Backscatter Communication (MBC)	29
2.4.3.2	Bistatic Backscatter Communication (BBC)	30
2.4.3.3	Ambient Backscatter Communication (AmBC)	30
2.4.3.4	Symbiotic Radio (SR)	30
3	Channel Shaping using RIS: From Diagonal Model to Beyond	31
3.1	Introduction	31
3.2	Beyond-Diagonal-Reconfigurable Intelligent Surface Model	33
3.3	Channel Singular Values Redistribution	35
3.3.1	A Toy Example	35
3.3.2	Pareto Frontier Characterization	37
3.3.3	Some Analytical Bounds	39
3.4	Achievable Rate Maximization	42
3.4.1	Alternating Optimization	42
3.4.2	Low-Complexity Solution	43
3.5	MIMO-IC	44
3.5.1	Leakage Interference Minimization	44
3.5.2	Weighted Sum-Rate Maximization	45
3.6	Simulation Results	47
3.6.1	Channel Singular Values Redistribution	49
3.6.1.1	Pareto Frontier	49
3.6.1.2	Analytical Bounds and Numerical Results	50
3.6.2	Achievable Rate Maximization	52
3.7	Conclusion	54

4	Appendix	55
4.1	Proofs for Chapter 3	55
4.1.1	Proof of Lemma 1	55
4.1.2	Proof of Proposition 1	56
4.1.3	Proof of Proposition 2	56
4.1.4	Proof of Proposition 3	57
4.1.5	Proof of Lemma 2	57
4.1.6	Proof of Proposition 4	58
	References	61

List of figures

1.1	A typical architecture of RIS. Source: Modified from [1].	4
2.1	Refraction in negative and positive-index materials. Incident and refracted rays stay at the same side of the normal axis in a negative-index material. . .	10
2.2	Wave and energy have opposite directions in a negative-index material. . . .	10
2.3	Refraction through metamaterials. For negative-index material, beams diverging from a point source is set in reverse and converges back to another point.	11
2.4	Reflection through metamaterials. Yellow dots represent scattering elements. Solid and dashed lines denote wavefronts and rays, respectively. The scattering elements work together to manipulate the phases of incident waves, resulting in a focused beam steered in the intended direction.	12
2.5	Network model of a 4-element RIS with (a) independent scattering and (b) fully cooperative scattering with all elements interconnected. Source: Modified from [2].	14
2.6	Network model of an 8-element RIS with group-wise cooperative scattering of group size (a) 2 and (b) 4. The group size is a design parameter to balance the circuit complexity and scattering performance. Source: Modified from [2].	15
2.7	Block diagram of a closed-loop RIS-aided Wireless Power Transfer (WPT).	18
2.8	Equivalent circuit of (a) rectenna and (b) single-diode half-wave rectifier. .	19
2.9	Information and energy flows in SWIPT and BackCom systems. The blue and black parts denote information and power subsystems, respectively. . .	24
2.10	Architectures of a co-located SWIPT receiver.	25
2.11	Illustration of scattering applications. The blue flows denote the primary link while the magenta flows denote the backscatter link.	29
3.1	$2 \times 2 \times 2$ (no direct) channel singular value shaping by diagonal and symmetry unitary RIS.	36

3.2	Average leakage interference versus RIS elements N^S and group size L . Transmitters and receivers are randomly generated in a disk of radius 50 m centered at the RIS. $(N^T, N^R, N^E, K) = (8, 4, 3, 5)$, $(\gamma^D, \gamma^F, \gamma^B) = (3, 2.4, 2.4)$, and reference pathloss at 1 m is -30 dB.	46
3.3	Average weighted sum-rate versus Signal-to-Noise Ratio (SNR), RIS elements N^S and group size L . $(N^T, N^R, N^E, K) = (8, 4, 3, 5)$, $(\Lambda^D, \Lambda^F, \Lambda^B) = (65, 54, 46)$ dB, $\rho_k = 1, \forall k$	47
3.4	Average weighted sum-rate versus user pairs K , RIS elements N^S and group size L at SNR = 15 dB. $(N^T, N^R, N^E) = (4, 4, 3)$, $\rho_k = 1, \forall k$	48
3.5	Pareto frontiers of singular values of a 2T2R channel reshaped by a RIS. . .	49
3.6	Achievable channel singular values: analytical bounds (green lines) and numerical optimization results (blue and red bars). ‘D’ means diagonal RIS and ‘BD’ means fully-connected BD-RIS. ‘rank- k ’ refers to the forward channel.	50
3.7	Average maximum channel power versus BD-RIS group size and MIMO dimensions. ‘Cascaded’ refers to the available power of the cascaded channel, i.e., the sum of (sorted) element-wise power product of backward and forward subchannels.	51
3.8	Average maximum channel power versus RIS configuration. ‘OP-left’ and ‘OP-right’ refer to the suboptimal solutions to problem (3.28) by lossy transformation (3.30) where Θ is to the left and right of the product, respectively.	52
3.9	Average achievable rate versus MIMO and RIS configurations. The noise power is $\eta = -75$ dB, corresponding to a direct SNR of -10 to 30 dB. ‘Alternate’ refers to the alternating optimization and ‘Decouple’ refers to the low-complexity design. ‘D’ means diagonal RIS and ‘BD’ means fully-connected BD-RIS.	53

List of tables

3.1 Average Performance of BD-RIS Designs 48

Abbreviations

bpcu	bits per channel use
bps/Hz	bits per second per Hertz
AF	Amplify-and-Forward
AI	Artificial Intelligence
AM	Arithmetic Mean
AmBC	Ambient Backscatter Communication
AO	Alternating Optimization
AP	Access Point
AWGN	Additive White Gaussian Noise
BackCom	Backscatter Communication
BBC	Bistatic Backscatter Communication
BCD	Block Coordinate Descent
BD	Beyond-Diagonal
BER	Bit Error Rate
BIBO	Binary-Input Binary-Output
BLE	Bluetooth Low Energy
BLS	Backtracking Line Search
CLT	Central Limit Theorem
CP	Canonical Polyadic
CR	Cognitive Radio
CSCG	Circularly Symmetric Complex Gaussian
CSI	Channel State Information
CSIT	Channel State Information at the Transmitter
CSS	Chirp Spread Spectrum
CW	Continuous Waveform

DC	Direct Current
DCMC	Discrete-input Continuous-output Memoryless Channel
DF	Decode-and-Forward
DMC	Discrete Memoryless Channel
DMMAC	Discrete Memoryless Multiple Access Channel
DMTC	Discrete Memoryless Thresholding Channel
DoF	Degree of Freedom
DP	Dynamic Programming
DSSS	Direct-Sequence Spread Spectrum
EIRP	Effective Isotropic Radiated Power
eMBB	enhanced Mobile Broadband
FDMA	Frequency-Division Multiple Access
FPGA	Field-Programmable Gate Array
FS	Frequency-Selective
FSK	Frequency-Shift Keying
FSSS	Frequency-Hopping Spread Spectrum
GM	Geometric Mean
GP	Geometric Programming
i.i.d.	independent and identically distributed
IC	Interference Channel
IM	Index Modulation
IoE	Internet of Everything
IoT	Internet of Things
KKT	Karush-Kuhn-Tucker
LC	Low-Complexity
LEH	Linear Energy Harvester
LoRa	Long Range
LoRaWAN	Long Range Wide Area Network
LoS	Line-of-Sight

M2M	Machine-to-Machine
MAC	Multiple Access Channel
MBC	Monostatic Backscatter Communication
MC	Multiplication Coding
MIMO	Multiple-Input Multiple-Output
MISO	Multiple-Input Single-Output
ML	Maximum-Likelihood
MMSE	Minimum Mean-Square-Error
mMTC	massive Machine-Type Communication
MRC	Maximal Ratio Combining
MRT	Maximum Ratio Transmission
MSE	Mean-Square Error
NLoS	Non-Line-of-Sight
NOMA	Non-Orthogonal Multiple Access
NRZ	Non-Return-to-Zero
OFDM	Orthogonal Frequency-Division Multiplexing
PAE	Power-Added Efficiency
PAPR	Peak-to-Average Power Ratio
PC	Point-to-point Channel
PDF	Probability Density Function
PGA	Projected Gradient Ascent
PIN	Positive Intrinsic Negative
PS	Power Splitting
PSK	Phase Shift Keying
QAM	Quadrature Amplitude Modulation
QoS	Quality of Service
R-E	Rate-Energy
RCG	Riemannian Conjugate Gradient
RF	Radio-Frequency
RFID	Radio-Frequency Identification

RIS	Reconfigurable Intelligent Surface
RZ	Return-to-Zero
SC	Superposition Coding
SCA	Successive Convex Approximation
SDMA	Space-Division Multiple Access
SDP	Semi-Definite Programming
SDR	Semi-Definite Relaxation
SIC	Successive Interference Cancellation
SIMO	Single-Input Multiple-Output
SINR	Signal-to-Interference-plus-Noise Ratio
SISO	Single-Input Single-Output
SMAWK	Shor-Moran-Aggarwal-Wilber-Klawe
SMF	Scaled Matched Filter
SNR	Signal-to-Noise Ratio
SR	Symbiotic Radio
STAR	Simultaneous Transmission and Reflection
SVD	Singular Value Decomposition
SWIPT	Simultaneous Wireless Information and Power Transfer
TDMA	Time-Division Multiple Access
TS	Time Switching
UE	User Equipment
URLLC	Ultra-Reliable Low-Latency Communication
WF	Water-Filling
WIT	Wireless Information Transfer
WPCN	Wireless Powered Communication Network
WPT	Wireless Power Transfer
WSN	Wireless Sensor Network
WSR	Weighted Sum-Rate
ZF	Zero-Forcing

Notation

Constants

e	Euler's number $\simeq 2.71828 \dots$
j	Imaginary unit $= \sqrt{-1}$
π	Archimedes' constant $\simeq 3.14159 \dots$

Objects

a, A	Scalar
\mathbf{a}	Column vector
\mathbf{A}	Matrix
\mathcal{A}	Finite set
$\mathbf{0}$	All-zero matrix
$\mathbf{1}$	All-one matrix
\mathbf{I}	Identity matrix

Sets

\mathbb{N}	Natural numbers (excluding 0)
\mathbb{R}	Real numbers
\mathbb{R}_+	Real nonnegative numbers
\mathbb{C}	Complex numbers
\mathbb{I}	Probability domain $[0, 1]$
$\mathbb{H}_+^{n \times n}$	Positive semi-definite matrices of dimension $n \times n$
$\mathbb{U}^{n \times n}$	Unitary matrices of dimension $n \times n$

Operations

$(\cdot)^*$	Complex conjugate
$(\cdot)^T$	Transpose
$(\cdot)^H$	Hermitian (conjugate transpose)

$(\cdot)^\dagger$	Moore-Penrose inverse
$(\cdot)^+$	Ramp function $\max(0, \cdot)$
$ \cdot $	Absolute value of a complex number
$\ \cdot\ $	Euclidean norm of a vector
$\ \cdot\ _F$	Frobenius norm of a matrix
$\arg(\cdot)$	Argument of a complex number
$\text{card}(\cdot)$	Cardinality of a finite set
$\log(\cdot)$	Natural logarithm of a real number
$\exp(\cdot)$	Exponential of a scalar or square matrix
$\text{tr}(\cdot)$	Trace of a square matrix
$\det(\cdot)$	Determinant of a square matrix
$\text{sv}(\cdot)$	Singular values sorted from largest to smallest
$\text{diag}(\cdot)$	Constructs a square matrix with inputs on the main diagonal
$\text{diag}^{-1}(\cdot)$	Retrieves the main diagonal of a square matrix
$\Re(\cdot)$	Retrieves the real part of a complex number
$\Im(\cdot)$	Retrieves the imaginary part of a complex number
$\mathbb{E}(\cdot)$	Expectation operator
$\mathbb{A}(\cdot)$	Extracts the Direct Current component of a signal
\odot	Hadamard product
\otimes	Kronecker product
$(\cdot)_{[x:y]}$	Shortcut for $(\cdot)_x, (\cdot)_{x+1}, \dots, (\cdot)_y$

Distributions

\sim	Follows a distribution
$\mathcal{CN}(\mathbf{0}, \Sigma)$	Multivariate Circularly Symmetric Complex Gaussian with covariance Σ

Subscripts

$(\cdot)_D$	Direct
$(\cdot)_F$	Forward
$(\cdot)_B$	Backward
$(\cdot)_I$	Information
$(\cdot)_P$	Power
$(\cdot)_T$	Transmit
$(\cdot)_S$	Scatter
$(\cdot)_R$	Receive

Superscripts

$(\cdot)^{(r)}$	r -th iterated value
$(\cdot)^*$	Stationary point

Chapter 1

Introduction

1.1 Motivation

The quest for better wireless connectivity has been long-standing since Marconi's illuminating radio in 1895. Great successes have been made at the transmitter and receiver sides over the past century, and the communications society is unprecedentedly close to the Shannon limit [3]. By 2025, global mobile data traffic is expected to reach 607 exabytes per year [4] while the number of connected devices may exceed 75 billion [5]. At the same time, wireless applications are also evolving in various forms to address world-changing incidents like COVID-19, climate change, geopolitical tensions, and Artificial Intelligence (AI) revolution. An initial attempt was made in 5G where the network prioritizes among high-throughput, ubiquitous-coverage, high-reliability, low-latency, massive-connectivity, and energy-efficient services [6]. However, the desire of human and machine for better communication shows no signs of slowing down. Emerging applications such as smart cities, autonomous driving, telemedicine, extended reality, federated learning, and generative intelligence are calling for a stronger and smarter wireless infrastructure. It is envisioned that 6G will be designed to meet the following requirements [7–9]:

- *Throughput:* The network would be able to provide a peak data rate of 1 Tbps and an average data rate of 100 Gbps per user.
- *Latency:* Sub-millisecond end-to-end latency would be achieved for low-latency applications like autonomous driving and remote surgery.
- *Reliability:* A success rate of 99.9999% would be guaranteed for ultra-reliable applications like industrial automation and cooperative robotics.

- *Connectivity*: The number of connected devices per kilometer square would be increased to 10 million for supporting Internet of Everything (IoE).
- *Mobility*: Commercial airlines with a maximal velocity of 1000 km/h would be the target application scenario.
- *Energy efficiency*: Power consumption has been a major criticism for 5G. It is expected that energy per bit would be reduced by over 90% in 6G to reduce carbon footprints.
- *Positioning accuracy*: Thanks to THz base stations, a 3D positioning accuracy of centimeter level may be achieved for indoor and outdoor environments.
- *Coverage*: Poor coverage has been another bottleneck for 5G. A terrestrial-satellite-aerial integrated network would provide a ubiquitous and uniform coverage for urban, rural, and remote areas.
- *Security and privacy*: Physical-layer security can be improved with narrower beams at higher frequencies and destructive scattering at the environment. Privacy can be enhanced with federated learning and homomorphic encryption.

Beyond the statistical requirements above, the next-generation wireless network is desired to integrate human, machine, environment, and AI seamlessly for a harmonic ecosphere. This paradigm shift from *connectivity* to *intelligence* is fueled by the latest advances in machine learning (theory) and programmable metamaterials (hardware). The former enables the network to understand the environment while the latter evolves the environment from a chaotic medium to a conscious agent that can serve on demand. Together, they form a symbiotic relationship with the potential to revolutionize how the world energize, sense, communicate, and interact.

One promising candidate within this 6G vision is Reconfigurable Intelligent Surface (RIS), a programmable metasurface that recycles and redistributes the electromagnetic waves in the air for improved wireless performance. It could be incorporated into the transmitter and receiver for *beamforming*, employed as a free-rider information source for *modulation*, or simply placed in space as a standalone device for *channel shaping*. These applications have distinctive requirements and trade-offs, but the operation principles are the same and those roles are not mutually exclusive. Imagine a future where everything can be “smartened” by coating with a metamaterial layer and attaching a microcontroller tag. Only a few active radiating sources (like the sun) are needed, while most objects (like the universe) can exploit the surrounding waves to energize themselves, sense the environment, communicate with others, and help those in need when idle. This vision motivates three research questions to be addressed in this thesis:

- *How does RIS impact different wireless applications such as communication and far-field power transfer?*
- *Is it possible to integrate RIS with other scattering applications into a versatile tool that blurs the boundary between the network and environment?*
- *What is the ultimate limit of channel reshaping through passive RIS and what are the implications on transceiver designs?*

Before delving into these questions, we first provide a short overview of RIS and introduce some potential applications. A detailed literature review and technical discussion on RIS and other technologies will be reserved for Chapter 2.

1.2 Overview on Reconfigurable Intelligent Surface (RIS)

1.2.1 Concept

RIS is commonly known as a planar surface involving numerous wave scattering elements (a.k.a. unit cells, reflective patches), whose amplitude and phase responses can be engineered in real-time to achieve a desired radiation pattern. It behaves like a delicate Radio-Frequency (RF) mirror with adjustable curvature and orientation, which allows the incident signals to be focused and redirected in a particular direction. As shown in Fig. 1.1, its typical architecture consists of three stacked layers and a controller [1]. The top layer is a two-dimensional array of scattering elements printed on a dielectric substrate. The elements directly interact with the impinging waves, which are usually fabricated from metamaterial or patch/dipole antennas with sub-wavelength dimension and spacing. The middle layer is a copper ground plate that provides voltage reference and avoids signal leakage. The bottom layer is a circuit board that associate each element with adjustable components, such as varactor and Positive Intrinsic Negative (PIN) diodes [10]. It also hosts a Field-Programmable Gate Array (FPGA) controller that controls the circuit and coordinate with transceivers in the network. By adjusting the scatter response of all elements, the RIS can effectively manipulate the wavefront for a constructive or destructive superposition and thus improve the ambient wireless environment.

1.2.2 Characteristics

The key characteristics of RIS are summarized as follows:

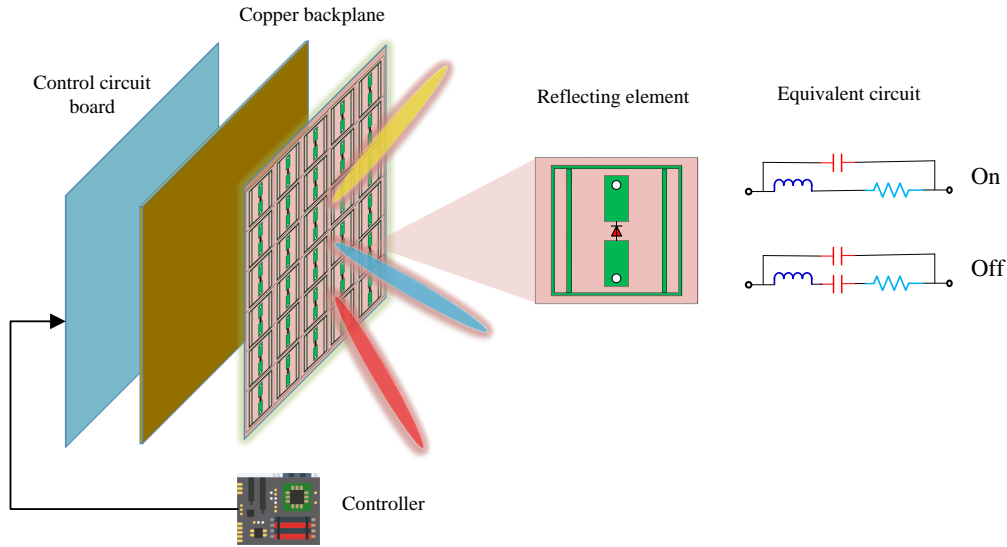


Fig. 1.1 A typical architecture of RIS. Source: Modified from [1].

- *Passive and environmental-friendly:* RIS reflects the incident waves in a passive manner and does not require dedicated RF chains.¹ This is different from Amplify-and-Forward (AF) relays that require power-hungry oscillators and introduces additional thermal noise.
- *Flexible:* It provides a software configurable environment that can be adapted for different applications and scenarios. This is different from conventional reflectarray [11] and frequency selective surfaces [12] with predefined radiation patterns and frequency response.
- *Full-duplex and universal:* This physical-layer solution can simultaneously support communication, sensing, and power transfer without self-interference. Thanks to channel reciprocity, the optimal configuration for downlink and uplink coincide with each other [13]. This is different from Decode-and-Forward (DF) relays that are designed for a specific communication link and suffers from packet delays.
- *Low-cost and conformal:* It can be manufactured from low-cost materials and deployed in various forms (e.g., walls, windows, ceilings, tables) to provide seamless coverage and powerful customization for indoor and outdoor environments. This is different from conventional multi-antenna systems that features complex hardware and bulky structures.

¹The controller may be implemented with low-power components and powered by ambient energy.

1.2.3 Applications

The channel manipulation capability of RIS unlocks a wide range of unprecedented applications, such as signal enhancement [14], interference suppression [15], blockage bypassing [16], coverage extension [17], and security control [18]. It also has the potential to convey additional information [19], compensate for the Doppler effect [20], transform frequency-selective channels into frequency-flat [21], improve the spatial diversity for multi-antenna systems [22], and create artificial time diversity for multi-user orthogonal [23] and non-orthogonal [24] multiple accesses.

Those fancy characteristics and applications of RIS have also attracted significant attention from the industry. The first public testing attempt was made in 2018 by NTT Docomo and Metawave, which demonstrated a metasurface reflectarray in the FR2 band of 5G can boost a downlink data rate from 60 Mbps to 560 Mbps [25]. Later in 2020, NTT Docomo developed a transparent dynamic RIS that can allow 28GHz signals to reflect or pass through with negligible power loss. A regional “RIS alliance” was formed in 2021 by Chinese companies and institutes including ZTE, China Mobile, and CAICT, which soon released a white paper [26] to promote the technology and standardization. In December 2022, ITU-R drafted a recommendation report for IMT-2030 (6G) [27] that marks RIS as a key technology to enhance the radio interface for multiple physical dimension transmission. These developments showcase the rapid progress of RIS from theoretical concept to practical implementation, paving the way for its integration into the next-generation network.

1.3 Outline and Contributions

The thesis is outlined as follows:

- Chapter 1 provides an overview of the thesis. It introduces the motivation and objectives, raise critical research questions, discusses the characteristics and applications of RIS, and summarizes the contributions of each research chapter. A list of publications is also provided.
- Chapter 2 provides necessary background knowledge for RIS, Wireless Power Transfer (WPT), Simultaneous Wireless Information and Power Transfer (SWIPT), and Backscatter Communication (BackCom). It covers fundamental principles, hardware implementation, signal and system models, performance metrics, design challenges, and state-of-the-art research.

- Chapter ?? investigate the impact of RIS on wireless information and power transfer. The key contributions include:
 - Introduce RIS to a multi-antenna multi-carrier SWIPT system with different receiver architectures;
 - Consider joint waveform and beamforming design for the proposed system under a practical energy harvester model;
 - Characterize the Rate-Energy (R-E) performance trade-off by maximizing harvested energy subject to different communication rate constraints;
 - Propose local-optimal and low-complexity algorithms and evaluate their narrow and wideband performance through numerical simulations;
 - Discuss the array gain for communication and the scaling order for power transfer in terms of the number of transmit antennas and RIS elements.
- Chapter ?? develops a novel scatter protocol that integrates beamforming and modulation. The key contributions include:
 - Provide an in-depth comparison of RIS with state-of-the-art BackCom technologies and discuss the key properties of active and passive transmissions coexisting systems;
 - Unify RIS and BackCom as one battery-free cognitive radio called RIScatter, where dispersed or co-located scatter nodes ride over an active primary link to modulate their own information and engineering the legacy channel simultaneously;
 - Integrate backscatter modulation and passive beamforming seamlessly into the input distribution design that allows arbitrary trade-off in between;
 - Propose a low-complexity cooperative receiver that sequentially decodes both coexisting links and exploits backscatter detection as part of channel training;
 - Characterize the achievable primary-backscatter rate region over different designs of input distribution at the scatter nodes, active beamforming at the Access Point (AP), and energy detector at the receiver;
 - Discuss the impact of practical factors such as the number of scatter nodes and states, transmit antenna size, backscatter symbol duration, and Signal-to-Noise Ratio (SNR) on the system performance.
- Chapter 3 explores the ultimate channel shaping capabilities of RIS in Multiple-Input Multiple-Output (MIMO) systems. The key contributions include:

- Quantify the capability of a passive RIS to reshape the MIMO Point-to-point Channel (PC) in terms of singular values via analytical bounds and numerical optimization;
- Focus on a general Beyond-Diagonal (BD)-RIS architecture featuring element-wise connections and demonstrate its superior signal processing performance (subspace alignment and subchannel rearrangement) over the widely-adopted diagonal model;
- Propose an efficient Riemannian Conjugate Gradient (RCG) algorithm for general BD-RIS optimization and provide low-complexity solutions for quadratic problems;
- Characterize the Pareto frontiers of channel singular values and obtain power- and rate-optimal BD-RIS configurations in MIMO PC;
- Investigate the impact of BD-RIS on leakage interference suppression and Weighted Sum-Rate (WSR) maximization in MIMO Interference Channel (IC);
- Discuss how channel shaping helps to decouple joint RIS-transceiver designs with comparable performance and significantly reduced complexity.

1.4 Publications

- Y. Zhao, B. Clerckx, and Z. Feng, “IRS-aided SWIPT: Joint waveform, active and passive beamforming design under nonlinear harvester model,” *IEEE Transactions on Communications*, vol. 70, pp. 1345–1359, 2022
- Y. Zhao and B. Clerckx, “Riscatter: Unifying backscatter communication and reconfigurable intelligent surface,” 12 2022
- —, *RIS in Wireless Information and Power Transfer*. John Wiley & Sons, Ltd, 2023, pp. 271–295
- Y. Zhao, H. Li, M. Franceschetti, and B. Clerckx, “Channel shaping using reconfigurable intelligent surfaces: From diagonal to beyond,” *To be submitted to IEEE Transactions on Wireless Communications*

Chapter 2

Background

This chapter provides essential background for topics covered in the thesis. A detailed literature review will be presented within each research chapter.

2.1 Reconfigurable Intelligent Surface (RIS)

2.1.1 Programmable Metamaterials

Metamaterials refer to artificial structures engineered for unusual properties that may not be found in nature. The concept was initially proposed by Victor Veselago in 1967, who conjectured the existence of mediums with negative dielectric constant $\epsilon < 0$ and negative permeability $\mu < 0$ [32]. Such metamaterials are known as “negative-index” because the refraction index is defined as the *negative* square root $n = -\sqrt{\epsilon\mu} < 0$, in order to be consistent with Maxwell’s equations. It was not until 1999 that their feasibility was experimentally demonstrated by John Pendry at Imperial College using split-ring resonators [33]. Since then, metamaterials have attracted significant interests due to their counterintuitive properties, to name a few:

- *Negative refraction:* As shown in Fig. 2.1a, the incident and refracted rays stay at the same side of the normal axis [32]. This phenomenon is in contrast to the usual refraction but can still be predicted from Snell’s law

$$\frac{\sin \theta_1}{\sin \theta_2} = n. \quad (2.1)$$

It is worth mentioning that a generalized law of refraction and refraction has been proposed in [34], which has become a standard reference for the design and analysis of metamaterials.

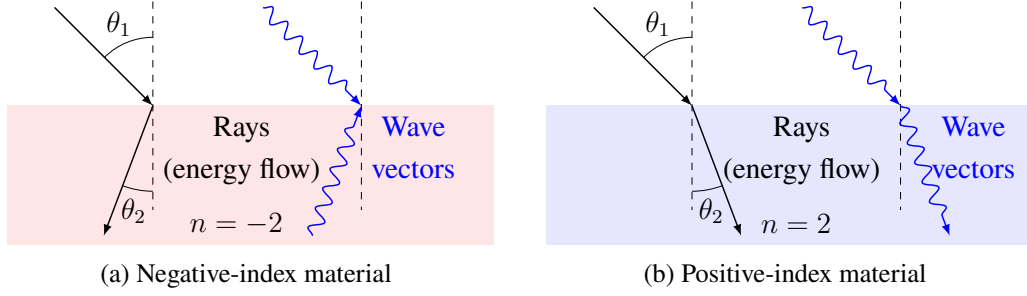


Fig. 2.1 Refraction in negative and positive-index materials. Incident and refracted rays stay at the same side of the normal axis in a negative-index material.

- *Opposite wave direction:* As shown in Fig. 2.2a, the wave vector and energy flow (indicated by the Poynting vector) are opposite to each other in a negative-index material [35]. This can be inferred from the electric field equation

$$\vec{E} = \vec{E}_0 \exp(jkz - j\omega t) \quad (2.2)$$

where $k = k_0 n < 0$ is the wavenumber, \vec{E}_0 and k_0 are the free-space electric field and wavenumber reference, z is the propagation distance, ω is the angular frequency, and t is the time. Negative-index materials are thus also called “left-hand” because the propagation direction of the electric and magnetic fields can be determined by a left-hand rule.

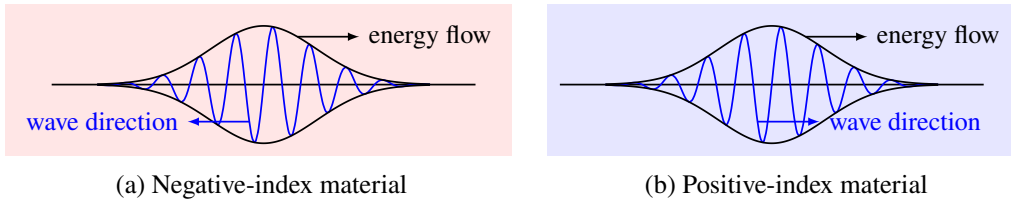


Fig. 2.2 Wave and energy have opposite directions in a negative-index material.

Conventional metamaterials have fixed properties that depend on the geometry and arrangement of their constituent elements. Once fabricated, these properties cannot be easily changed unless the structure is physically altered. This limits their early usage to military and defense, with applications such as invisibility cloaks and optical illusions. In 2014, the concept of “coding” and “programmable” metamaterials was validated by researchers at Southeast University [36], who realized digital control of radar cross-section using biased diodes and FPGA. With a proper model of the target properties and external citation, the

metamaterial can be reconfigured in real-time for desired behaviors. For example, a self-adaptive metasurface equipped with motion and light sensors have been developed in [37] for single- and multi-beam steering.

Next, we discuss the principles of electromagnetic wave redirection via refraction and reflection:

- *Refraction:* As shown in Fig. 2.3a, the negative-index material can re-focus the beams diverging from a point source to another point behind the material [38]. This could be helpful for wireless applications where the transmitter and receiver are at different sides of the material.
- *Reflection:* As shown in Fig. 2.4b, the scattering elements cooperatively alter the phase of the incident wave for a constructive (or destructive) superposition of the reflected waves in the target direction [39]. This could be helpful for wireless applications where the transmitter and receiver are at the same side of the material.

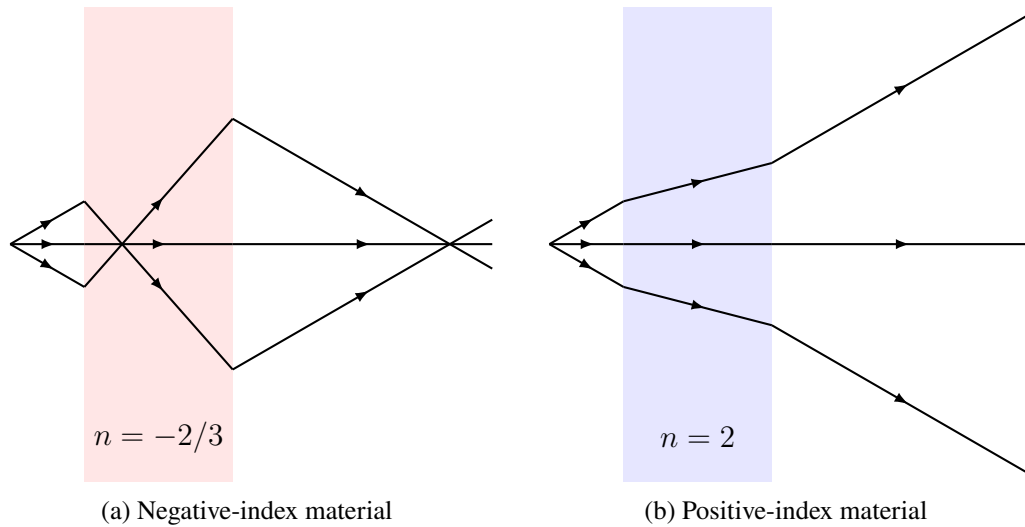


Fig. 2.3 Refraction through metamaterials. For negative-index material, beams diverging from a point source is set in reverse and converges back to another point.

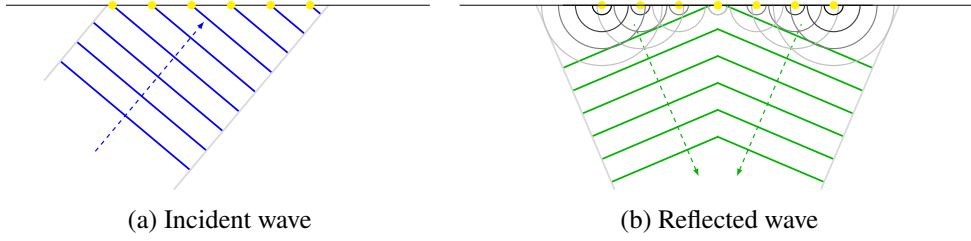


Fig. 2.4 Reflection through metamaterials. Yellow dots represent scattering elements. Solid and dashed lines denote wavefronts and rays, respectively. The scattering elements work together to manipulate the phases of incident waves, resulting in a focused beam steered in the intended direction.

It is worth noticing that refraction and reflection are different implementations of *passive beamforming* where the phase and amplitude of the ambient signal are altered by the metamaterial for a desired net effect. In the next subsection, we will some typical RIS scattering models and their physical architecture.

2.1.2 Wave Scattering Models

2.1.2.1 Principles

RF wave can be manipulated by scattering elements made from *programmable metamaterials* or *passive antennas* [40]. As discussed above, the former refracts or reflects the incident signals at the air-cell boundary and mainly applies a phase shift. In contrast, the latter allows the wave to feed into and collect from the antenna port such that some energy can be absorbed by the circuit and the rest is reradiated to the space. An interesting observation is that when excited by an external wave, a scattering element can simultaneously function as an object and a radiator. The corresponding scattered field is [41]

$$\vec{E}_{\text{scatter}}(Z_L) = \underbrace{\vec{E}_{\text{structural}}}_{\text{structural component}} + \underbrace{\Gamma I_M \vec{E}_{\text{antenna}}}_{\text{antenna component}}, \quad (2.3)$$

where Z_L is the load impedance, $\vec{E}_{\text{structural}}$ is the residual field under perfect matching (i.e., modelling as an object), \vec{E}_{antenna} is the radiated field with unit current at the terminal and no external excitation (i.e., modelling as a radiator), I_M is the current under perfect matching, and Γ is the reflection coefficient

$$\Gamma = \frac{Z_L - Z_0^*}{Z_L + Z_0}, \quad (2.4)$$

and Z_0 is the characteristic impedance for programmable metamaterials or the input impedance for passive antennas. It is worth mentioning that

- *Structural component*: Depends on the geometry and material of the scatterer. It is usually modelled as part of the environment multipath [42, 43] or simply regarded a Direct Current (DC) offset when the impinging signal is Continuous Waveform (CW) [44].
- *Antenna component*: Depends on the reflection coefficient that can be altered by load impedance. This is widely exploited for various scattering applications, such as backscatter modulation in BackCom and passive beamforming in RIS [29].

We then introduce two canonical RIS models that will be adopted in the work chapters. More accurate models based on field equations (e.g., [45, 46]) and measurement fitting (e.g., [47]) are also available in the literature.

2.1.2.2 Diagonal Phase Shift Model

A straightforward way to model the RIS scattering effect is to consider independent scattering elements with purely reactive load impedance [48]. The reflection coefficient of the n -th element is thus

$$\theta_n = \frac{jX_n - Z^*}{jX_n + Z} = \exp(j\phi_n), \quad (2.5)$$

where X_n is the reactance and ϕ_n is the phase shift on the scattered wave. For a total of N_S elements, the RIS scattering matrix is *diagonal with complex unit-magnitude entries*

$$\mathbf{\Theta} = \text{diag}(\theta_1, \dots, \theta_{N_S}) = \begin{bmatrix} \theta_1 & 0 & \cdots & 0 \\ 0 & \theta_2 & \cdots & 0 \\ \vdots & \vdots & \ddots & \vdots \\ 0 & 0 & \cdots & \theta_{N_S} \end{bmatrix}. \quad (2.6)$$

Despite the strong assumptions, this diagonal phase shift model is widely used for the analysis of RIS systems due to its simplicity and analytical tractability.

2.1.2.3 Beyond-Diagonal (BD) Model

How to model the RIS response if the passive scattering elements can be cooperative instead of independent? This question has been answered by [2] where a BD model was proposed. From a network theory perspective [49], the interaction between the scattering elements can be modelled as lossless (but not necessarily symmetric) in-group connections in an N_S -port

circuit network, as shown in Figs. 2.5 and 2.6 [2]. This architecture allows wave impinging on any element to propagate within the circuit and depart partially from other elements in the same group.

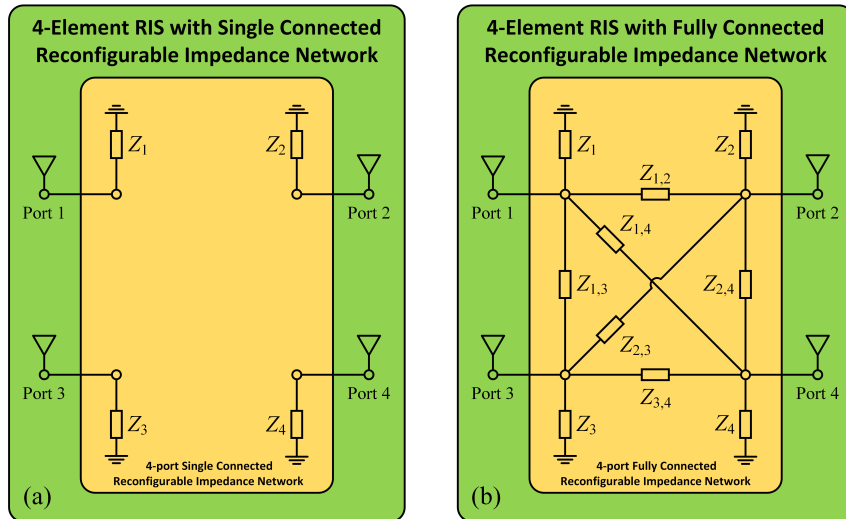


Fig. 2.5 Network model of a 4-element RIS with (a) independent scattering and (b) fully cooperative scattering with all elements interconnected. Source: Modified from [2].

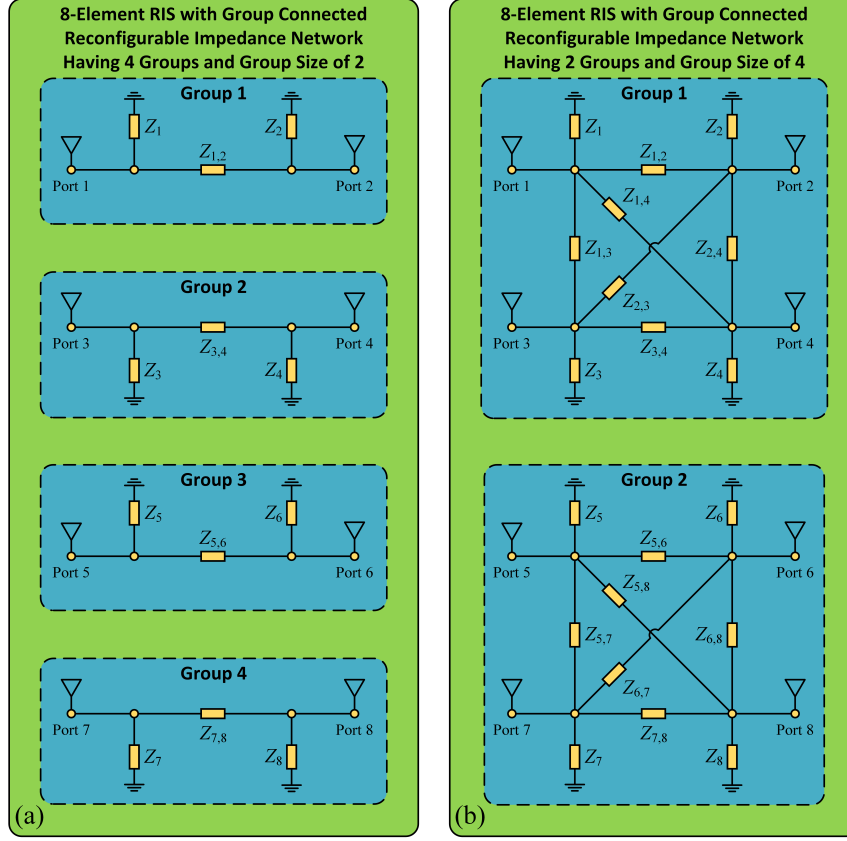


Fig. 2.6 Network model of an 8-element RIS with group-wise cooperative scattering of group size (a) 2 and (b) 4. The group size is a design parameter to balance the circuit complexity and scattering performance. Source: Modified from [2].

A general BD-RIS can be modeled as an N_S -port network that divides into G individual groups, each containing $L \triangleq N_S/G$ elements interconnected by real-time reconfigurable connections. With symmetric components (e.g., capacitors and inductors), the scattering matrix of group $g \in \mathcal{G} \triangleq \{1, \dots, G\}$ is [2]

$$\Theta_g = (j\mathbf{X}_g + Z_0\mathbf{I})^{-1}(j\mathbf{X}_g - Z_0\mathbf{I}), \quad (2.7)$$

which satisfies both *symmetric* and *unitary* properties

$$\Theta_g = \Theta_g^T, \quad (2.8a)$$

$$\Theta_g^H \Theta_g = \mathbf{I}. \quad (2.8b)$$

On the other hand, lossless networks may also be built over asymmetric passive components (e.g., ring hybrids and branch-line hybrids) [50] such that the symmetric constraint (2.8a)

can be relaxed. This corresponds to the ultimate passive model where energy conservation (2.8b) is the only constraint for each group, as widely considered in quantum physics. The overall scattering matrix of asymmetric BD-RIS is thus *block-diagonal with unitary blocks*

$$\Theta = \text{diag}(\Theta_1, \dots, \Theta_G) = \begin{bmatrix} \Theta_1 & \mathbf{0} & \cdots & \mathbf{0} \\ \mathbf{0} & \Theta_2 & \cdots & \mathbf{0} \\ \vdots & \vdots & \ddots & \vdots \\ \mathbf{0} & \mathbf{0} & \cdots & \Theta_G \end{bmatrix}, \quad (2.9)$$

where (2.8b) is equivalently denoted as $\Theta_g \in \mathbb{U}^{L \times L}$. The group size L is a design parameter to balance the circuit complexity and scattering performance. Diagonal (single-connected) and unitary (fully-connected) RIS can be viewed as extreme cases with group size $L = 1$ and $L = N_S$, respectively. Therefore, the BD model (2.9) is envisioned to be the next-generation theoretical foundation for passive RIS, which grants more design freedom and stronger signal processing capability.

It is also worth mentioning that each group can be abstracted as a mathematical graph with L vertices and a variable number of edges [51]. One element is in the same group with another if and only if there is at least one path (via edges) between them. It implies that instead of connecting every pair of elements, the practical circuit can be designed to have a sparse graph with only a few connections, which is beneficial for reducing the circuit complexity and power loss from non-ideal components. Antenna directivity and radiation pattern should also be modelled in the scattering matrix, especially when the locations of users or RIS are not fixed. This has motivated the concept of Simultaneous Transmission and Reflection (STAR)-RIS [52, 53] and multi-sector RIS [54] where incident wave is partially steered to various directions for different users.

2.2 Wireless Power Transfer (WPT)

2.2.1 Introduction

Wireless devices are becoming smarter as well as more energy-efficient and eco-friendly. Koomey's law [55] predicts the computing efficiency roughly doubles every 19 months and the amount of power needed for the same operation decreases to 1% in a decade. Over the past 15 years, the rise of low-power technologies like Wireless Sensor Network (WSN) and Internet of Things (IoT) have hatched life-changing applications including smart homes, digital healthcare, and industrial automation. Today, Radio-Frequency Identification (RFID) tags and basic sensors (e.g., thermometer and proximeter) can operate on microwatts of power

[56, 57], while communication protocols like Bluetooth Low Energy (BLE) and Long Range Wide Area Network (LoRaWAN) only consume tens of milliwatts [58]. This low-power trend together with the upsurge of mobile devices is calling for a *truly wireless* energy solution that eliminates the need for periodic cable plugging or battery replacement. While great successes have been witnessed for candidates like solar and piezoelectric, their prospects in wireless systems remain unclear due to the bulky converter, unpredictable source, and limited operation range. One promising solution on the horizon is WPT through electromagnetic waves. It can be classified into two categories based on the operation principle [59]:

- *Non-radiative near-field*: Power is transferred over a short distance (typically a few centimeters) by inductive coupling between coils or capacitive coupling between electrodes in a field-to-field manner. The former has been widely standardized (e.g., Qi 2.0) and commercialized (e.g., wireless charging pads), while the latter is still in the research stage.
- *Radiative far-field*: Power is transferred over a long distance (typically a few meters) by directional microwave or laser beams between antennas in a point-to-point manner. It shares many similarities with RF communication (e.g., infrastructure and wireless environment) but suffers from lower energy efficiency than non-radiative WPT due to pathloss.

Radiative WPT¹ brings numerous opportunities to future wireless networks. First, it completely eliminates wired connections and can be integrated into existing wireless systems with minimum modifications. Those properties translate to simple deployment, high scalability, and low maintenance cost. Second, the power can be simultaneously radiated to multiple devices on demand in a predictable, sustainable and reliable manner. This supports our initial vision and is different from other uncontrollable and intermittent energy sources. Third and most importantly, radio waves carries power and information simultaneously. WPT can therefore be jointly designed with Wireless Information Transfer (WIT) to make the most of radiation, spectrum and infrastructures. However, energy efficiency and safety concerns have been two major obstacles that limit the practical development of WPT. In Section 2.3, we will discuss how RIS can help address these issues.

¹In the following part of the thesis, WPT refers to radiative WPT.

2.2.2 Modules and Coupling Effect

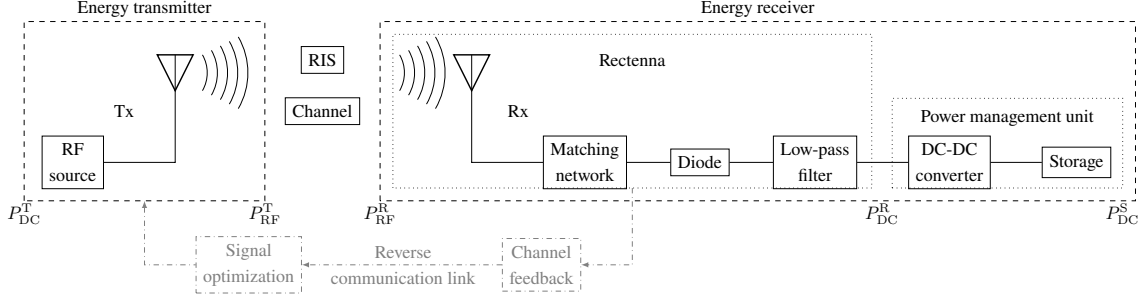


Fig. 2.7 Block diagram of a closed-loop RIS-aided WPT.

The block diagram a closed-loop RIS-aided WPT system is illustrated in Fig. 2.7. The RF signal is generated and radiated by the energy transmitter, propagated through a wireless channel in the presence of a RIS, captured by the antenna(s) at the receiver, converted to DC power by rectifier(s), then passed to the power management unit. Upon successful harvesting, the DC power is either delivered directly to the device or stored in a battery/super capacitor for future operations. When a feedback link is available, one can acquire Channel State Information (CSI) at the energy transmitter and exploit it for signal optimization. Such a closed-loop RIS-aided WPT system can provide a complete control of transmitter, channel, and receiver, which is essential for maximizing the end-to-end power transfer efficiency

$$\eta = \frac{P_{DC}^S}{P_{DC}^T} = \underbrace{\frac{P_{RF}^T}{P_{DC}^T}}_{\eta_1} \underbrace{\frac{P_{RF}^R}{P_{RF}^T}}_{\eta_2} \underbrace{\frac{P_{DC}^R}{P_{RF}^R}}_{\eta_3} \underbrace{\frac{P_{DC}^S}{P_{DC}^R}}_{\eta_4}, \quad (2.10)$$

where P_{DC}^T is the transmitted DC power, P_{RF}^T is the transmitted RF power, P_{RF}^R is the received RF power, P_{DC}^R is the received DC power, and P_{DC}^S is the stored DC power. The power conversion efficiencies are specified below:

- η_1 : Transmitter DC-to-RF conversion efficiency² that depends on the RF power amplifier and transmit antenna. It is also called “drain efficiency” and state-of-the-art designs can achieve $\eta_1 \geq 70\%$ [61].
- η_2 : Channel RF-to-RF conversion efficiency that depends on the wireless environment and RIS configuration. This is the major bottleneck of WPT since the radiated power is inversely proportional to the propagation distance squared.

²This is different from Power-Added Efficiency (PAE) used in amplifier rating, which takes into account both DC power and input waveform power [60].

- η_3 : Receiver RF-to-DC conversion efficiency that depends on the impedance matching and rectifier design. We will discuss its behavior and modelling in the next subsection.
- η_4 : Storage DC-to-DC conversion efficiency that depends on the converter circuit and battery characteristics. Modern power management units can achieve a charging efficiency $\eta_4 \geq 90\%$ [62].

It is worth mentioning that η_1 and η_3 also depend on the characteristics of input waveform like power level, carrier frequency, and Peak-to-Average Power Ratio (PAPR) [63]. Extensive efforts have been contributed from RF, wireless communications, and power electronic communities to improve the conversion efficiency of individual modules. However, it is often overlooked in the literature that a practical WPT system is highly *non-linear* since the amplifier and rectifier are very sensitive to the input waveform. This non-linear behavior can lead to a *coupling effect* between the modules, such that optimizing η_1 to η_4 independently does not necessarily maximize the end-to-end power efficiency η [63]. Besides, the system modeling and analysis are subject to practical constraints like diode threshold and reverse-breakdown voltages, device parasitics, impedance mismatch, and harmonic generation [64].

2.2.3 Non-Linear Harvester Behavior

2.2.3.1 Equivalent Circuits

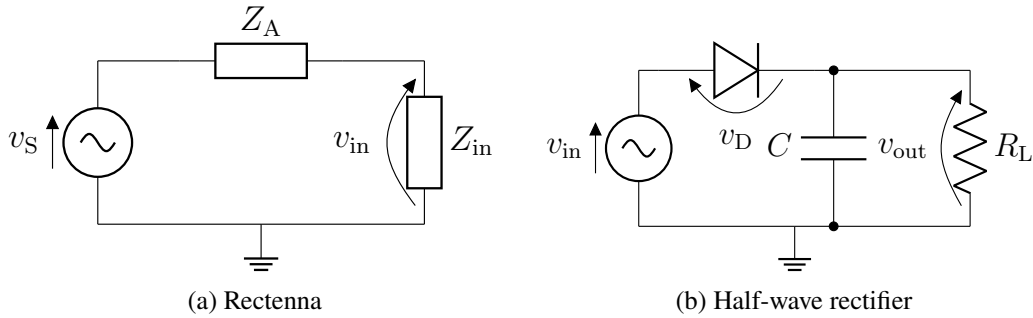


Fig. 2.8 Equivalent circuit of (a) rectenna and (b) single-diode half-wave rectifier.

The rectifier is a nonlinear circuit that converts the RF signal to DC power by rectifying and filtering the input signal. Figs. 2.8 illustrates the equivalent circuits of a rectenna (antenna and rectifier) and a single-diode half-wave rectifier, where v_S is the source voltage on the receive antenna, $Z_A = R_A + jX_A$ is the antenna impedance, $Z_{in} = R_{in} + jX_{in}$ is the total impedance of the matching network and rectifier, v_{in} is input voltage on the matching network and rectifier, v_D is the diode voltage, C is the buffer capacitance, R_L is the rectifier

load resistance, and v_{out} is the output voltage. It is worth mentioning that the half-wave rectifier is the most popular choice in WPT literature due to its simple behavior and low cost. Other rectifier topologies like full-wave, bridge, and voltage doubler can potentially improve the RF-to-DC conversion efficiency [65], but their modeling and analysis are much more complicated.

2.2.3.2 Operation Regions and Signal Models

The diode is the key non-linear component that determines to the harvested energy. Generally speaking, the behavior of any rectenna can be separated into three operation regions [63]:

- *Linear region:* When the input power level is relatively low, the output power is proportional to the input and the RF-to-DC conversion efficiency η_3 is a constant. Most early WPT research (especially from communications society) assume the rectenna works in this region. For a received signal $y(t)$, the harvested DC power in this region can be modelled as

$$P_{\text{DC}}^{\text{R}} = \eta_3 P_{\text{RF}}^{\text{R}} = \eta_3 \mathbb{A}\{|y(t)|^2\}, \quad (2.11)$$

which suggests that maximizing the received RF signal power is sufficient to maximize the harvested DC power.

- *Non-linear (transition) region:* When the input power level is moderate, the output power increases *exponentially* with the input and η_3 is significantly higher than the linear region. This is the most interesting region that can be exploited to improve the overall power efficiency. For a tractable model, consider a perfectly matched ($Z_{\text{in}} = Z_{\text{A}}^*$) half-wave rectifier in Fig. 2.8(b) and assume the voltage across the matching network is negligible. The received RF power is totally transferred to the rectifier input $P_{\text{RF}}^{\text{R}} = \mathbb{E}\{|y(t)|^2\} = \mathbb{E}\{|v_{\text{in}}(t)|^2/R_{\text{in}}\} = \mathbb{E}\{|v_{\text{in}}(t)|^2/R_{\text{A}}\}$ such that the voltage sources can be expressed in terms of the received signal [63]

$$v_{\text{in}}(t) = y(t)\sqrt{R_{\text{A}}}, \quad v_{\text{S}}(t) = 2y(t)\sqrt{R_{\text{A}}}. \quad (2.12)$$

The current passing through the diode is given by the characteristic equation $i_{\text{D}}(t) = I_{\text{S}}(\exp(v_{\text{D}}(t)/nv_{\text{T}}) - 1)$, where I_{S} is the reverse bias saturation current, v_{T} is the thermal voltage, and n is the ideality factor. Its Taylor expansion around the steady point $-v_{\text{out}}$ is [63]

$$i_{\text{D}}(t) = \sum_{i=0}^{\infty} k_i (v_{\text{D}}(t) + v_{\text{out}})^i = \sum_{i=0}^{\infty} k_i v_{\text{in}}^i(t) = \sum_{i=0}^{\infty} k_i R_{\text{A}}^{i/2} y^i(t), \quad (2.13)$$

where $k_0 = I_S(\exp(-v_{\text{out}}/nv_T) - 1)$, $k_i = I_S \frac{\exp(-v_{\text{out}}/nv_T)}{i!(nv_T)^i}$ for $k \in \mathbb{N}$. The rectifier output DC current can be written as a function of the received signal

$$i_{\text{out}} = \sum_{i=0}^{\infty} k_i R_A^{i/2} \mathbb{A}\{y^i(t)\} = \sum_{i=0, \text{even}}^{\infty} k_i R_A^{i/2} \mathbb{A}\{y^i(t)\} \quad (2.14)$$

where the second equality is because $\mathbb{A}\{y^i(t)\} = 0$ for odd i . Note that the dependency of k_i on $-v_{\text{out}} = -i_{\text{out}} R_L$ makes it nontrivial to formulate a closed-form expression for the harvested DC power. Fortunately, it is shown in [63] that maximizing the harvested DC power is equivalent to maximizing the quantity

$$z \triangleq \sum_{i=2, \text{even}}^{n_0} \beta_i \mathbb{A}\{y^i(t)\}, \quad (2.15)$$

where $\beta_i = I_S \frac{R_A^{i/2}}{i!(nv_T)^i}$ is a constant and n_0 is the truncation order. Selecting $n_0 = 2$ yields the same result as (2.11), which suggests that the linear model is a special case of the more accurate non-linear model. For a moderate excitation, the contribution of higher-order terms is significant and should be modelled in the harvested DC power.

- *Saturation region:* When the input power level is too high, the diode works in the reverse breakdown region, the rectifier is saturated, and the output power is a constant. This is the region where the η_3 significantly drops and should be avoided by circuit design. For a fixed rectenna with Gaussian input signal, a parametric model was proposed in [66]

$$P_{\text{DC}}^{\text{R}} = \frac{\Psi_{\text{DC}} - P_{\text{sat}} \Omega}{1 - \Omega}, \quad \Psi_{\text{DC}} = \frac{P_{\text{sat}}}{1 + \exp(-a(P_{\text{RF}}^{\text{R}} - b))}, \quad \Omega = \frac{1}{1 + \exp(ab)}, \quad (2.16)$$

where the constant P_{sat} denotes the maximum harvested power when the rectifier is saturated, and the constants a and b model the nonlinear charging rate with respect to input power and the minimum turn-on voltage of the rectifier, respectively. Parameters P_{sat} , a , and b can be obtained by curve fitting over measurement results.

The exact boundaries between those regions depend on the rectifier circuit and input waveform [67]. Signals with a higher PAPR usually exhibit the nonlinear and saturation effects at lower input power levels. For example, the nonlinear region is typically $[-20, 0]$ dBm for a CW and $[-30, -10]$ dBm for a multisine [68]. This not only motivates adaptive multi-carrier waveform designs [63, 67, 69, 70] but also calls for a joint optimization of the transmitter, channel (via RIS), and receiver to improve the end-to-end power efficiency.

2.3 Simultaneous Wireless Information and Power Transfer (SWIPT)

2.3.1 Introduction

WIT and WPT have been treated separately over the past century and have made significant progress in their respective fields. Interestingly, electromagnetic waves carry information and energy simultaneously and the same signal can be used for communication and power transfer. The idea of SWIPT was first proposed in 2008 [71] and has since attracted significant attention from both academia and industry. It is a promising solution to connect and energize trillions of low-power mobile devices, providing power at microwatt level and coverage up to tens of meters in a unified manner [72]. SWIPT can also smoothly shift between the two extreme cases to fully exploit the RF spectrum and network infrastructure. It is envisioned that future network providers will be able to offer a complete wireless solution including data and power services, which is essential for the upcoming intelligent era.

One of the most important issues in SWIPT is that the energy harvester requires a much higher received signal power (several orders of magnitude) than the information decoder [73]. Since the channel RF-to-RF efficiency η_2 is the primary constraint on the overall power efficiency, how to combat the pathloss and fading effects has been recognized as a crucial research topic for WPT SWIPT. Fortunately, this issue can be effectively mitigated by introducing a RIS to the environment. By carefully tuning the scatter response of the RIS elements, one can potentially achieve the following benefits:

- *Energy focusing:* The scattered waves can be steered towards the receivers or focused on a dedicated “hotspot zone” to increase the harvester input power level. This is also helpful to extend the coverage and improve the reliability of the energy link.
- *Beam splitting:* Instead of transmitting one strong beam towards each user, the energy signal can be split into multiple weaker beams rerouted by the RIS to even out the spatial power distribution. This is useful to bypass physical obstacles (especially in high-frequency and large-scale networks) and reduce the health risk of radiation.

RIS can also be used to assist the information link by SNR enhancement and interference suppression, as mentioned in subsection 1.2.3.

2.3.2 Rate-Energy (R-E) Tradeoff

Despite WIT and WPT share many similarities, their difference in design objectives, system architectures, and practical constraints make a joint implementation of SWIPT particularly challenging. Some preference of WIT and WPT are inherently conflicting, for example:

- *Waveform and modulation:* Under an average power constraint, WIT favors Gaussian signaling with maximum entropy distribution [74] while WPT prefers deterministic (unmodulated) multisine with higher PAPR [75].
- *Channel:* In a MIMO scenario, WIT favors full-rank Non-Line-of-Sight (NLoS) with high spatial diversity while WPT prefers rank-deficient Line-of-Sight (LoS) with high spatial correlation [76].
- *Receiver:* The power sensitivity is usually in the range of -40 to -80 dBm for information receivers and -10 to -30 dBm for energy harvesters [77].

Those disparities translate to a fundamental trade-off between information and power transfer in SWIPT systems, which is often quantified by a *R-E region*.

$$\mathcal{C}_{R-E}(P) \triangleq \left\{ (r, e) : 0 \leq r \leq \log(1 + \gamma), 0 \leq e \leq z \right\}, \quad (2.17)$$

where P is the average transmit power, γ is the SNR at the information decoder, and z defined in (2.15) is uniquely mapped to the harvested DC power. Each point in this region corresponds to a *rate-energy pair* achieved by a particular *resource allocation scheme*. It is worth mentioning that different transceive strategies (e.g., waveform and receiver design) can lead to totally different R-E regions (instead of different points in the same region), which motivates a joint optimization of the transmitter, channel, and receiver.

2.3.3 Modules and Operation Modes

2.3.3.1 Information and Energy Flows

In SWIPT, the information and energy are always transmitted from the same source while their receivers can be either co-located or separated, as shown in Figs. 2.9(a) and 2.9(b). This is different from BackCom where the energy is delivered in the downlink and the information is sent in the uplink, as shown in Figs. 2.9(c) and 2.9(d).

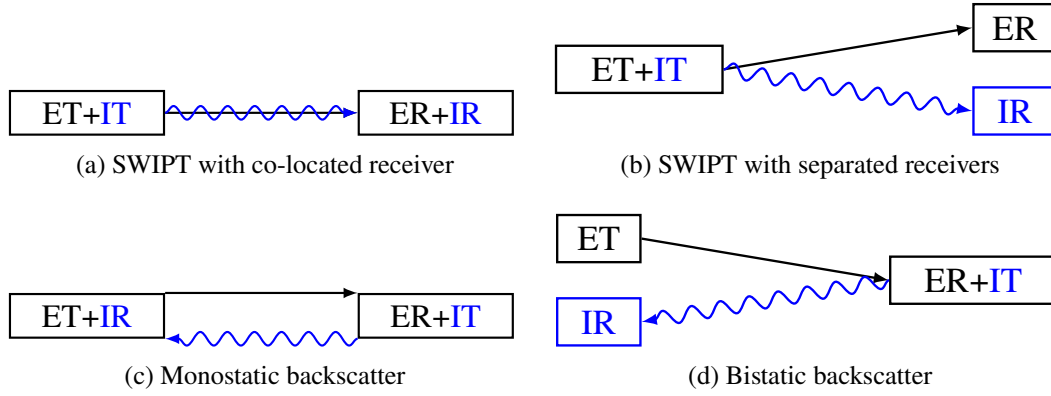
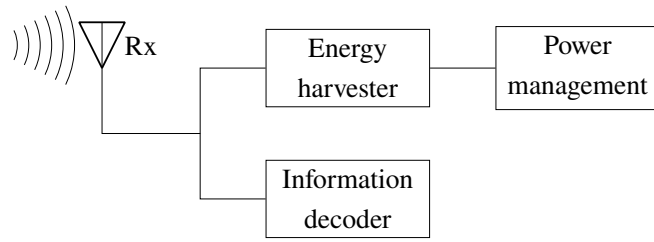


Fig. 2.9 Information and energy flows in SWIPT and BackCom systems. The blue and black parts denote information and power subsystems, respectively.

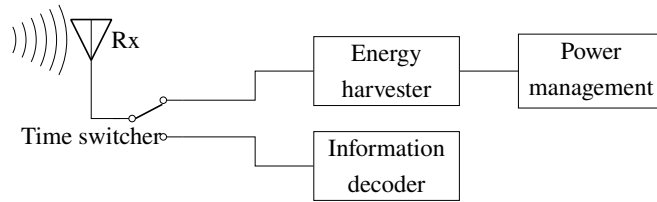
From a design perspective, co-located SWIPT receiver is a more general model since it can exploit the received signal for either purpose or a mixture in between. We thus focus on this model in the following context.

2.3.3.2 Receiver Architectures

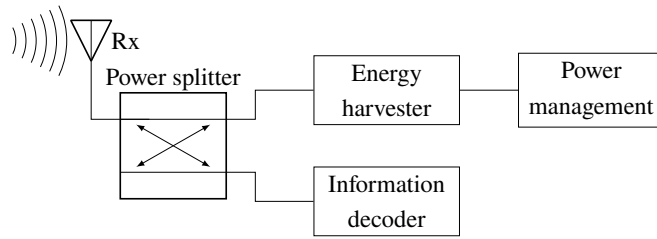
Figure 2.10 illustrates four potential architectures for a co-located SWIPT receiver [78]:



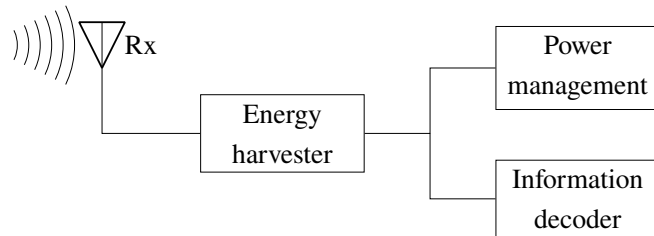
(a) Ideal receiver



(b) Time switching receiver



(c) Power splitting receiver



(d) Integrated receiver

Fig. 2.10 Architectures of a co-located SWIPT receiver.

- *Ideal receiver*: The received signal is used for both information decoding and energy harvesting. This is theoretically the most efficient design with a rectangle R-E region but is unimplementable in practice due to hardware constraints.
- *Time Switching (TS) receiver*: Each time block is divided into individual WIT and WPT phases, where the receiver switches between information decoder and energy harvester, respectively. The transmitted waveform and RIS response are optimized independently for each phase, and the resulting R-E region is a triangle with two vertices corresponding to WIT-only and WPT-only.

- *Power Splitting (PS) receiver*: The received signal is split into two parts with power ratio ρ and $1-\rho$. The former is fed into the energy harvester and the latter is used for information decoding. The transmitter and RIS are jointly optimized for both purposes with the knowledge of splitting ratio, and the resulting R-E region may be non-convex.
- *Integrated receiver [79]*: The transmit signal is modulated in properties that can be well-preserved after rectification (e.g., pulse position) such that information can be decoded from the energy harvester output.

The most popular architectures in the literature are TS and PS due to their practicality and tractability. The R-E region of the former can be inferred from that of the latter, since the WIT-only and WPT-only vertices in TS correspond to $\rho = 1$ and $\rho = 0$ in PS, respectively. Integrated receiver eliminates the need of RF chains and advanced architectures, but experiences information degradation and works better for low-throughput applications.

2.4 Backscatter Communication (BackCom)

2.4.1 Introduction

The scattered waves from any object inherently contain some information about the object. This contributed to the great success of radar in the World War II, where the “objective” information about the target (e.g., size, speed, and position) can be extracted from the reflected signal. Soon after the war in 1948, Stockman demonstrated the concept of BackCom where the target is no longer a dumb wave scatterer but part of the communication system that is willing to modulate its “subjective” information over the reflected signal [80]. The communication society quickly realized its potential to separate the power-hungry RF carrier emitter with the low-power information modulator, which is essential for miniaturizing wireless devices and increasing the network scale. As shown in Figs. 2.9(c) and 2.9(d) on Page 24, the backscatter node (a.k.a. tag) is activated by an energy signal (also functions as carrier) in the downlink and modulates over the scattered signal in the uplink. The energy transmitter (a.k.a. carrier emitter) and information receiver (a.k.a. reader) can be either co-located or separated, known respectively as monostatic and bistatic BackCom.

One of the most well-known BackCom applications is RFID which made its debut in the 1970s [81]. RFID readers send a query signal and exploit the reflected signal from nodes (attached to objects) to identify and track them. The nodes can be powered wirelessly by the impinging wave and does not have to be in the vicinity of the reader. It has been standardized in ISO/IEC 18000 and EPC Gen2 [82] and widely used in supply chain management, access

control, and asset tracking. On the other hand, BackCom also plays an important role in emerging applications like IoT, WSN, and Machine-to-Machine (M2M) communications. Their main difference to RFID is that the message is no longer a static identifier but can be dynamically sensed from the environment or generated on demand. This enables a new paradigm of self-sustainable, intelligent, and pervasive sensing and communication, which is a key building block for our initial vision.

Nevertheless, low throughput and limited coverage are acknowledged as two critical problems for conventional BackCom systems. Those are inevitably inherited from the nature of wave scattering — the radiated signal has to travel a round trip (emitter-node-reader) with double pathloss, while the scatter response is frequency-dependent and usually results in a narrow bandwidth. Monostatic BackCom is also subject to a strong self-interference that further degrades the error performance and achievable rate. Finally, the nodes are idle most of the time and only respond when externally inquired. This is in sharp contrast to RIS where the elements are contributing for channel enhancement all the time. To mitigate those issues, multi-antenna techniques and special modulation schemes are two promising solutions in the literature. For example, a multi-antenna carrier emitter can perform energy beamforming [83], a multi-antenna node can perform energy combining with spatial modulation [84, 85] or space-time coding [86], and a multi-antenna reader can perform coherent [87, 88] or non-coherent [89] detection. We will discuss some popular modulation and coding techniques for BackCom in the following subsection.

2.4.2 Modulation and Coding Schemes

BackCom and RIS share the same wave scattering model in Section 2.1.2.1, but the reflection coefficient Γ in (2.4) is exploited in different manners. The difference is two-fold:

- *Modulation requires variation:* BackCom relies on dynamically changing the reflection coefficient over time to encode information. This is different from RIS where the optimal configuration (and reflection coefficient) is fixed for a given channel realization.
- *Harvesting requires absorption:* Part of the impinging wave should be fed into the node to power its operation. This is different from RIS where a full reflection is desired to maximize its channel control capability.

Denote the amplitude scattering ratio of the BackCom node as α , i.e., the power absorption ratio is $(1 - \alpha)^2$. Some popular modulation schemes are summarized below:

- *Quadrature Amplitude Modulation (QAM) [90]*: The reflection coefficient corresponding to the m -th symbol is

$$\Gamma_m = \alpha \frac{c_m}{\max_{m'} |c_{m'}|} \quad (2.18)$$

where c_m is the corresponding constellation point. This scheme is simple but exhibits a low detection SNR especially when the constellation size is large.

- *Frequency-Shift Keying (FSK) [82]*: For 2-FSK, the reflection coefficient is

$$\Gamma(t) = \begin{cases} \alpha, & t \in \left[\frac{n}{\Delta f}, \frac{2n+1}{2\Delta f}\right) \\ -\alpha, & t \in \left[\frac{2n+1}{2\Delta f}, \frac{n+1}{\Delta f}\right) \end{cases} = \frac{\pi}{4} \sum_{m=1, \text{odd}}^{\infty} \frac{\alpha}{m} \sin(2\pi m \Delta f t), \quad (2.19)$$

where $n \in \mathbb{N}$. If the incident wave is a CW at frequency f_0 , the reflected signal is dominated by its first harmonic

$$s_1(t) = \frac{\alpha\pi}{2} \left(\sin(2\pi(f_0 + \Delta f)t) - \sin(2\pi(f_0 - \Delta f)t) \right). \quad (2.20)$$

That is, periodically switching the reflection coefficient at rate Δf results in a frequency shift $\pm \Delta f$ on the reflected signal. Practical implementations have been demonstrated on a variety of license-free protocols (e.g., HitchHike [91], Inter-Technology [92], Passive Wi-Fi [93], BLE-Backscatter [94]) where the mirror copy can be suppressed.

- *Chirp Spread Spectrum (CSS) [95]*: A chirp is a signal whose frequency increases or decreases over time. CSS uses wideband linear-frequency modulated chirps to encode information, which is from Direct-Sequence Spread Spectrum (DSSS) and Frequency-Hopping Spread Spectrum (FHSS) with pseudo-random sequences and FSK with discrete frequencies. In particular, $N + 1$ reflection coefficients of the same envelope are sequentially selected at a regular rate Δf , given by

$$\Gamma_n = \alpha \exp(j\phi_n), \quad n \in \{0, 1, \dots, N\}, \quad (2.21)$$

where $\phi_n = \frac{2\pi}{\Delta f}(An^2 + Bn)$ and A, B are constants. As the core modulation scheme in Long Range (LoRa), it is more robust to noise and interference (with a reception sensitivity of -149 dBm), harder to be detected by eavesdroppers, and can be used for ranging and localization [82].

Common BackCom channel coding schemes include unipolar Return-to-Zero (RZ) and Non-Return-to-Zero (NRZ), Manchester, differential, pulse-pause and FM0. They are not the focus of the thesis and the readers are referred to [96, Chapter 2.3] for details.

2.4.3 Applications

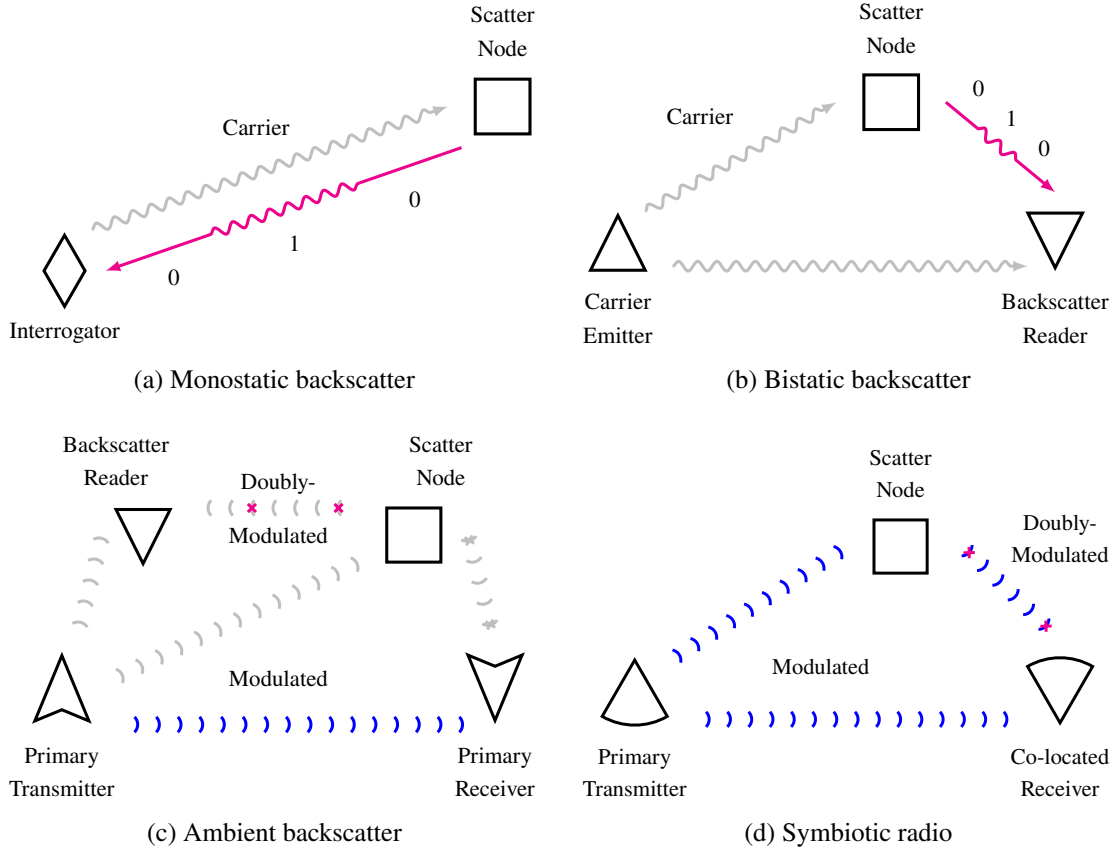


Fig. 2.11 Illustration of scattering applications. The blue flows denote the primary link while the magenta flows denote the backscatter link.

2.4.3.1 Monostatic Backscatter Communication (MBC)

Monostatic Backscatter Communication (MBC) is the most common architecture where the carrier emitter and reader are integrated into one device called interrogator. As shown in 2.9(c) and 2.11(a), the interrogator transmits a CW in the downlink and receives the reflected information-bearing signal in the uplink. The node varies its load impedance over time to switch between two states. Ideally, a full absorption (perfect matching, $\Gamma_0 = 0$) maps to bit “0” where energy is harvested, and a full reflection (perfect mismatch, $|\Gamma_1| = 1$) maps to bit “1” where SNR is determined. MBC is widely used in RFID systems. The integrated transceiver design reduces the hardware cost but suffers from strong self-interference and limited coverage.

2.4.3.2 Bistatic Backscatter Communication (BBC)

Bistatic Backscatter Communication (BBC) separates the carrier emitter and reader into two individual devices, as illustrated in 2.9(d) and 2.11(b). This helps to combat self-interference and extend the operation range, but the system involves three devices and requires more complex coordination and synchronization. It is more popular in more complicated scenarios like WSN and IoT with potentially moving nodes.

2.4.3.3 Ambient Backscatter Communication (AmBC)

Ambient Backscatter Communication (AmBC) has been recognized as a revolutionary technology since its debut in 2013 [97]. As shown in 2.11(c), it gets rid of dedicated RF sources and relies on ambient signals (e.g., TV, FM, and Wi-Fi) for both energy harvesting and information transfer. Compared with MBC and BBC, its carrier waveform is no longer a CW but a mixture of already modulated signals with different frequencies and amplitudes, which makes the detection more challenging. Therefore, it often employs FSK modulation to shift the scattered signals to a different band for reduced interference on both coexisting systems. AmBC is a plug-and-play and environmental-friendly IoT solution, but its practical deployment is limited by the availability and quality of ambient signals.

2.4.3.4 Symbiotic Radio (SR)

Symbiotic Radio (SR) is a relatively new concept proposed in 2019 that introduced itself as “cooperative AmBC” [98]. As shown in 2.11(d), it shares not only the transmitter, RF source, but also the receiver with a primary transmission. This is different from traditional AmBC where the legacy system can be unaware of the backscatter link and the node wants to minimize its footprint. Such a symbiotic interaction can improve the reliability of the backscatter link as well as the energy efficiency of the primary link, but unavoidably challenges the system design. For example, the acquisition of backscatter CSI can be difficult due to its passive characteristic, the detection of node message may involve complicated signal processing like Successive Interference Cancellation (SIC), and the synchronization of both links can be nontrivial due to the load-switching constraints. If those issues can be mitigated, SR would be a win-win solution that supercharges resource-constrained devices by leveraging the existing network infrastructure.

Chapter 3

Channel Shaping using RIS: From Diagonal Model to Beyond

3.1 Introduction

Today we are witnessing a paradigm shift from connectivity to intelligence, where the wireless environment is no longer a chaotic medium but a conscious agent that serves on demand. This is empowered by the recent advances in RIS, a real-time programmable metasurface of numerous non-resonant sub-wavelength scattering elements. It can manipulate the amplitude, phase, frequency, and polarization of the scattered waves [99] with a higher energy efficiency, lower cost, lighter footprint, and greater scalability than relays. Using RIS for passive beamforming has attracted significant interest in wireless communication [14, 100–102], backscatter [103, 40], sensing [104, 105], and power transfer literature [106, 107, 28], reporting a second-order array gain and fourth-order power scaling law (with proper waveform). On the other hand, RIS also enables backscatter modulation by dynamically switching between different patterns, as already investigated [108, 109, 29] and prototyped [110, 111]. Despite fruitful outcomes, one critical unanswered question is the channel shaping capability: *To what extent can a passive RIS reshape the wireless channel?*

The answer depends heavily on the hardware architecture and scattering model. In diagonal RIS, each scattering element is tuned by a dedicated impedance and acts as an *individual* phase shifter [1]. The concept is generalized to BD-RIS [2, 112] which physically connects adjacent elements using passive components. This allows *cooperative* scattering — wave impinging on one element can propagate within the circuit and depart partially from any element in the same group. BD-RIS can thus control both amplitude and phase of the reflected wave, generalizing the scattering matrix from diagonal with unit-magnitude entries

(2.6) to block diagonal with unitary blocks (2.9). Its benefit has been recently shown in receive power maximization [113–115, 51], transmit power minimization [116], and rate maximization [116, 51, 117, 118, 54]. Practical issues such as channel estimation [119] and mutual coupling [120] have also been investigated. Therefore, BD-RIS is envisioned as the next generation channel shaper with stronger signal processing flexibility [121].

Channel shaping is different from passive beamforming discussed in Chapters ?? and ?? because RIS is exploited as a stand-alone device to modify the inherent properties of the wireless channel. This allows one to decouple the RIS-transceiver design and explore the fundamental limits of wave manipulation. Relevant design criteria can be roughly classified into two categories:

- *Singular value centric*: Focus on the singular values of the equivalent channel matrix, which are closely related to the channel capacity and the diversity-multiplexing trade-off. Relevant designs are more complicated since they involve the entire channel matrix.
- *Power centric*: Focus on the second-order characteristics of the channel matrix, which are useful in Multiple-Input Single-Output (MISO) but less informative in MIMO. Relevant designs are more practical and straightforward.

The former has been studied in terms of minimum singular value [122], effective rank [122, 123], condition number [124, 125] in PC, and degree of freedom [126–128] in IC. The latter has been studied in terms of channel power [14, 113, 114] in PC and leakage interference [129] in IC. Although the results are insightful, the big picture is far from complete since there exists neither a systematic channel shaping study nor a universal RIS optimization framework. To the best of our knowledge, the most general channel shaping scenario (BD-RIS-aided MIMO) has not been studied, and the great potential of BD-RIS has not been fully exploited or understood. This chapter aims for a comprehensive answer to the channel shaping question through theoretical analysis and numerical optimization. The contributions are summarized below.

First, we exploit the Riemannian geometry of the Stiefel manifold to design a novel geodesic¹ RCG algorithm for BD-RIS optimization. This method modified from [130, 131] not only features lower complexity and faster convergence than general non-geodesic approach [132, 133], but also fits arbitrary group size and any smooth RIS optimization problem. Specifically, block-wise rotational update is performed along the geodesics of the Stiefel manifold, which are expressed compactly by the exponential map [134]. This is the first work to tailor an efficient optimization framework for asymmetric BD-RIS.

¹A geodesic refers to the shortest path between two points in a Riemannian manifold.

Second, we quantify the capability of a BD-RIS to redistribute the singular values of MIMO-PC. The *Pareto frontiers* are characterized by optimizing the weighted sum of singular values, where the weights can be positive, zero, or negative. This problem is solved by the proposed geodesic RCG algorithm. The resulting achievable singular value region generalizes most relevant metrics and provides an intuitive channel shaping benchmark. We also demystify the BD-RIS gain from off-diagonal entries and derive some analytical singular value bounds for rank-deficient MIMO and fully-connected (a.k.a. unitary) RIS. This is the first work to comprehensively answer the channel shaping question and fully unveil the potential of BD-RIS.

Third, we tackle BD-RIS-aided MIMO-PC rate maximization with two solutions: a local-optimal approach through Alternating Optimization (AO) and a low-complexity approach over channel shaping. The former updates active and passive beamforming by eigenmode transmission and RCG algorithm, respectively. The latter suboptimally decouples both blocks, recasts the shaping problem as channel power maximization, and solves it iteratively in closed form. Interestingly, the gap in between vanishes as BD-RIS evolves from diagonal to unitary. It suggests channel shaping decouples the RIS-transceiver design and offers a promising low-complexity solution. This is the first work to discuss the implications of channel shaping in joint active-passive beamforming optimization.

Fourth, we extend the aforementioned approaches to MIMO-IC where the BD-RIS is used for leakage interference minimization and WSR maximization. In the former case, we update the receive combiner, transmit precoder, and scattering matrix iteratively in closed forms with optimality proof. In the latter case, we alternatively update the transmit precoder by bisection and the scattering matrix by RCG algorithm. We also compare the impact of RIS on PC and IC.

3.2 Beyond-Diagonal-Reconfigurable Intelligent Surface Model

Consider a BD-RIS aided point-to-point MIMO system with N_T , N_S , N_R transmit, scatter, and receive antennas, respectively. This configuration is denoted as $N_T \times N_S \times N_R$ in the following context. The BD-RIS can be modeled as an N_S -port network [49] that divides into G individual groups, each containing $L \triangleq N_S/G$ elements interconnected by real-time reconfigurable components [2]. To simplify the analysis, we assume a lossless asymmetric

network² without mutual coupling between scatter elements, as previously considered in [112, 54, 118]. The overall scattering matrix of the BD-RIS is

$$\Theta = \text{diag}(\Theta_1, \dots, \Theta_G), \quad (3.1)$$

where $\Theta_g \in \mathbb{U}^{L \times L}$ is a unitary matrix that describes the response of group $g \in \mathcal{G} \triangleq \{1, \dots, G\}$. That is, $\Theta_g^H \Theta_g = \mathbf{I}$. Note that diagonal (single-connected) and unitary (fully-connected) RIS can be regarded as its extreme cases with group size $L = 1$ and $L = N_S$, respectively. Some potential physical architectures of BD-RIS are illustrated in [2, Fig. 3], [54, Fig. 5], and [51, Fig. 2], where the radiation pattern and circuit topology have impacts on the scattering matrix.

Let $\mathbf{H}_D \in \mathbb{C}^{N_R \times N_T}$, $\mathbf{H}_B \in \mathbb{C}^{N_R \times N_S}$, $\mathbf{H}_F \in \mathbb{C}^{N_S \times N_T}$ denote the direct (transmitter-receiver), backward (RIS-receiver), and forward (transmitter-RIS) channels, respectively. The equivalent channel is a function of the scattering matrix

$$\mathbf{H} = \mathbf{H}_D + \mathbf{H}_B \Theta \mathbf{H}_F = \mathbf{H}_D + \sum_g \mathbf{H}_{B,g} \Theta_g \mathbf{H}_{F,g}, \quad (3.2)$$

where $\mathbf{H}_{B,g} \in \mathbb{C}^{N_R \times L}$ and $\mathbf{H}_{F,g} \in \mathbb{C}^{L \times N_T}$ are the backward and forward subchannels for RIS group g , corresponding to the $(g-1)L$ to gL columns of \mathbf{H}_B and rows of \mathbf{H}_F , respectively. Since unitary matrices constitute an algebraic group with respect to multiplication, the scattering matrix of group g can be decomposed as

$$\Theta_g = \mathbf{L}_g \mathbf{R}_g^H, \quad (3.3)$$

where $\mathbf{L}_g, \mathbf{R}_g \in \mathbb{U}^{L \times L}$ are two unitary factor matrices. Let $\mathbf{H}_{B,g} = \mathbf{U}_{B,g} \Sigma_{B,g} \mathbf{V}_{B,g}^H$ and $\mathbf{H}_{F,g} = \mathbf{U}_{F,g} \Sigma_{F,g} \mathbf{V}_{F,g}^H$ be the compact Singular Value Decomposition (SVD) of the backward and forward channels, respectively. The equivalent channel can thus be rewritten as

$$\mathbf{H} = \mathbf{H}_D + \sum_g \overbrace{\mathbf{U}_{B,g} \Sigma_{B,g} \underbrace{\mathbf{V}_{B,g}^H \mathbf{L}_g \mathbf{R}_g^H \mathbf{U}_{F,g}}_{\text{backward-forward}} \Sigma_{F,g} \mathbf{V}_{F,g}^H}_{\text{direct-indirect}}. \quad (3.4)$$

Remark 1. By analyzing (3.4), we conclude that channel shaping through BD-RIS creates two critical opportunities:

²While symmetric BD-RIS (involving capacitors and inductors) is often considered in the literature [2, 113–115, 51, 116–118], asymmetric BD-RIS can be built over reconfigurable asymmetric passive components (e.g., ring hybrids and branch-line hybrids) [50].

- **Subspace alignment:** each group can align the singular matrices of the backward-forward (intra-group, multiplicative) and the direct-indirect (inter-group, additive) channels. In Single-Input Single-Output (SISO), subspace alignment boils down to phase matching and the optimal scattering matrix of group g is

$$\Theta_g^* = \exp(j\arg(h_D)) \mathbf{V}_{B,g} \mathbf{U}_{F,g}^H, \quad (3.5)$$

where $\mathbf{V}_{B,g} = [\mathbf{h}_{B,g}/\|\mathbf{h}_{B,g}\|, \mathbf{N}_{B,g}]$, $\mathbf{U}_{F,g} = [\mathbf{h}_{F,g}/\|\mathbf{h}_{F,g}\|, \mathbf{N}_{F,g}]$, and $\mathbf{N}_{B,g}, \mathbf{N}_{F,g} \in \mathbb{C}^{L \times (L-1)}$ are the orthonormal bases of the null spaces of $\mathbf{h}_{B,g}$ and $\mathbf{h}_{F,g}$, respectively. Diagonal RIS is thus sufficient for perfect SISO phase matching (with empty null spaces), but its disadvantage in subspace alignment scales with MIMO dimensions, since each element can only apply a common phase shift to the “pinhole” indirect channel of size $N_R \times N_T$ passing through itself. Even if the BD-RIS is fully-connected, there still exists a trade-off between the direct-indirect and backward-forward alignments.

- **Subchannel rearrangement:** this unique property of BD-RIS allows each group to rearrange and combine the backward and forward subchannels by strength. In SISO, diagonal RIS provides a maximum indirect channel amplitude of $\sum_{n=1}^{N_S} |h_{B,n}| |h_{F,n}|$, while BD-RIS can generalize it to $\sum_{g=1}^G \sum_{l=1}^L |h_{B,\pi_{B,g}(l)}| |h_{F,\pi_{F,g}(l)}|$, where $\pi_{B,g}$ and $\pi_{F,g}$ are permutations of $\mathcal{L} \triangleq \{1, \dots, L\}$. By rearrangement inequality, the maximum is attained by pairing the l -th strongest backward and forward subchannels in each group. The advantage of BD-RIS in subchannel rearrangement scales with MIMO dimensions, since the number of subchannels associated with each group grows with $N_R \times N_T$.

3.3 Channel Singular Values Redistribution

3.3.1 A Toy Example

We first illustrate the channel shaping capabilities of different RIS by a toy example. Consider a $2 \times 2 \times 2$ setup where the direct link is blocked. The diagonal RIS is modeled by $\Theta_D = \text{diag}(e^{j\theta_1}, e^{j\theta_2})$ while the unitary BD-RIS has 4 independent angular parameters

$$\Theta_U = e^{j\phi} \begin{bmatrix} e^{j\alpha} \cos \psi & e^{j\beta} \sin \psi \\ -e^{-j\beta} \sin \psi & e^{-j\alpha} \cos \psi \end{bmatrix}. \quad (3.6)$$

In particular, ϕ has no impact on the singular value because $\text{sv}(e^{j\phi} \mathbf{A}) = \text{sv}(\mathbf{A})$. We also enforce symmetry by $\beta = \pi/2$ such that both architectures have the same number of angular parameters. Fig. 3.1 shows the channel singular values achieved by an exhaustive grid search

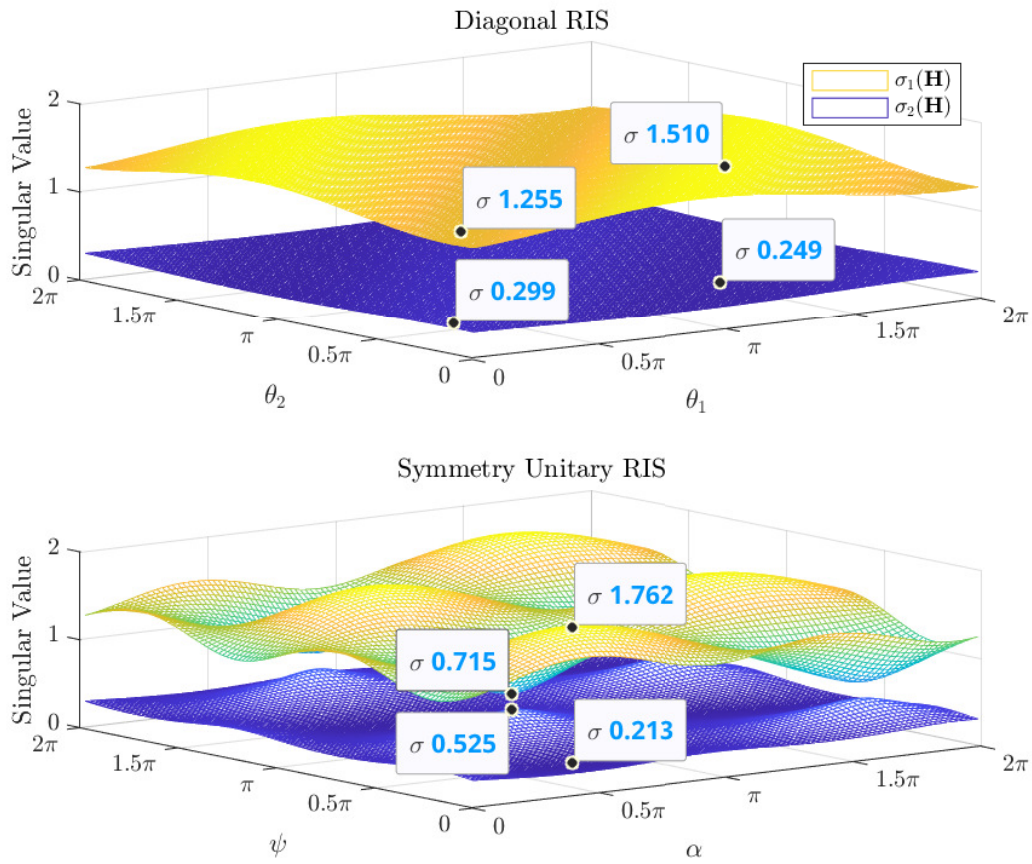


Fig. 3.1 $2 \times 2 \times 2$ (no direct) channel singular value shaping by diagonal and symmetry unitary RIS.

over (θ_1, θ_2) for diagonal RIS and (α, ψ) for symmetric unitary RIS. It is observed that both singular values can be manipulated up to 9% using diagonal RIS and 42% using symmetric BD-RIS, despite both architectures have the same number of scattering elements and design parameters. A larger performance gap is expected when asymmetric BD-RIS is available. This example shows BD-RIS can provide a wider dynamic range of channel singular values and motivates further studies on channel shaping.

3.3.2 Pareto Frontier Characterization

We then characterize the Pareto frontier of channel singular values by maximizing their weighted sum

$$\max_{\Theta} \sum_n \rho_n \sigma_n(\mathbf{H}) \quad (3.7a)$$

$$\text{s.t.} \quad \Theta_g^H \Theta_g = \mathbf{I}, \quad \forall g, \quad (3.7b)$$

where $n \in \{1, \dots, N \triangleq \min(N_T, N_R)\}$ and ρ_n is the weight of the n -th singular value that can be positive, zero, or negative. Varying $\{\rho_n\}$ unveils the entire achievable singular value region. Thus, the Pareto frontier problem (3.7) generalizes most relevant metrics and provides a powerful shaping framework. The objective (3.7a) is smooth in Θ and the feasible domain (3.7b) for group g corresponds to the Stiefel manifold. Next, we zoom out to general smooth maximization problems of asymmetric BD-RIS.

Inspired by [130, 131], we propose a block-wise RCG algorithm along the geodesics on the Lie group of unitary matrices $\mathbb{U}^{L \times L}$. It leverages the fact that unitary matrices are closed under multiplication. At iteration r , the gradient is computed in the Euclidean space and translated to the Riemannian manifold [132]

$$\nabla_{\mathbf{E},g}^{(r)} = \frac{\partial f(\Theta_g^{(r)})}{\partial \Theta_g^*}, \quad (3.8)$$

$$\nabla_{\mathbf{R},g}^{(r)} = \nabla_{\mathbf{E},g}^{(r)} \Theta_g^{(r)H} - \Theta_g^{(r)} \nabla_{\mathbf{E},g}^{(r)H}. \quad (3.9)$$

The Polak-Ribierre parameter [135] is approximated as [131]

$$\gamma_g^{(r)} = \frac{\text{tr}((\nabla_{\mathbf{R},g}^{(r)} - \nabla_{\mathbf{R},g}^{(r-1)}) \nabla_{\mathbf{R},g}^{(r)H})}{\text{tr}(\nabla_{\mathbf{R},g}^{(r-1)} \nabla_{\mathbf{R},g}^{(r-1)H})}, \quad (3.10)$$

and the conjugate direction is

$$\mathbf{D}_g^{(r)} = \nabla_{\mathbf{R},g}^{(r)} + \gamma_g^{(r)} \mathbf{D}_g^{(r-1)}. \quad (3.11)$$

In the Stiefel manifold, the geodesic emanating from $\Theta_g^{(r)}$ with velocity $\mathbf{D}_g^{(r)}$ and step size μ is described compactly by the exponential map [134]

$$\mathbf{G}_g^{(r)}(\mu) = \exp(\mu \mathbf{D}_g^{(r)}) \Theta_g^{(r)}. \quad (3.12)$$

An appropriate μ^* can be obtained by the Armijo rule [136].³ Finally, the scattering matrix is updated along the geodesic as

$$\Theta_g^{(r+1)} = \mathbf{G}_g^{(r)}(\mu^*). \quad (3.13)$$

Algorithm 1 summarizes the proposed block-wise geodesic RCG method for smooth maximization problems of asymmetric BD-RIS. Convergence to stationary points is guaranteed.

Remark 2. Compared with universal manifold optimization [132, 133], Algorithm 1 inherits a trifold benefit from [130, 131]:

1. No retraction thanks to rotational update (3.12), (3.13);
2. Lower computational complexity per iteration;
3. Faster convergence thanks to proper parameter space.

Lemma 1. The Euclidean gradient of (3.7a) w.r.t. BD-RIS group g is

$$\frac{\partial \sum_n \rho_n \sigma_n(\mathbf{H})}{\partial \Theta_g^*} = \mathbf{H}_{\mathbf{B},g}^H \mathbf{U} \text{diag}(\rho_1, \dots, \rho_N) \mathbf{V}^H \mathbf{H}_{\mathbf{F},g}^H, \quad (3.14)$$

where \mathbf{U} and \mathbf{V} are the left and right singular matrices of \mathbf{H} , respectively.

Proof. Please refer to Appendix 4.1.1. □

Algorithm 1 can thus be invoked for the Pareto singular value problem (3.7) where line 4 uses (3.14) explicitly.

³To double the step size, one only need to square the rotation matrix instead of recomputing the matrix exponential, i.e., $\exp(2\mu \mathbf{D}_g^{(r)}) = \exp^2(\mu \mathbf{D}_g^{(r)})$.

Algorithm 1 Block-wise geodesic RCG for asymmetric BD-RIS**Input:** $f(\Theta)$, G **Output:** Θ^*

```

1: Initialize  $r \leftarrow 0$ ,  $\Theta^{(0)}$ 
2: Repeat
3:   For  $g \leftarrow 1$  to  $G$ 
4:      $\nabla_{E,g}^{(r)} \leftarrow (3.8)$ 
5:      $\nabla_{R,g}^{(r)} \leftarrow (3.9)$ 
6:      $\gamma_g^{(r)} \leftarrow (3.10)$ 
7:      $\mathbf{D}_g^{(r)} \leftarrow (3.11)$ 
8:     If  $\Re\{\text{tr}(\mathbf{D}_g^{(r)\text{H}} \nabla_{R,g}^{(r)})\} < 0$  ▷ not an ascent direction
9:        $\mathbf{D}_g^{(r)} \leftarrow \nabla_{R,g}^{(r)}$ 
10:    End If
11:     $\mu \leftarrow 1$ 
12:     $\mathbf{G}_g^{(r)}(\mu) \leftarrow (3.12)$ 
13:    While  $f(\mathbf{G}_g^{(r)}(2\mu)) - f(\Theta_g^{(r)}) \geq \mu \cdot \text{tr}(\mathbf{D}_g^{(r)} \mathbf{D}_g^{(r)\text{H}})/2$ 
14:       $\mu \leftarrow 2\mu$ 
15:    End While
16:    While  $f(\mathbf{G}_g^{(r)}(\mu)) - f(\Theta_g^{(r)}) < \mu/2 \cdot \text{tr}(\mathbf{D}_g^{(r)} \mathbf{D}_g^{(r)\text{H}})/2$ 
17:       $\mu \leftarrow \mu/2$ 
18:    End While
19:     $\Theta_g^{(r+1)} \leftarrow (3.13)$ 
20:  End For
21:   $r \leftarrow r + 1$ 
22: Until  $|f(\Theta^{(r)}) - f(\Theta^{(r-1)})|/f(\Theta^{(r-1)}) \leq \epsilon$ 

```

3.3.3 Some Analytical Bounds

We then discuss some analytical bounds related to channel singular values.

Proposition 1 (degree of freedom). *In point-to-point MIMO, BD-RIS cannot achieve a higher Degree of Freedom (DoF) than diagonal RIS.*

Proof. Please refer to Appendix 4.1.2. □

Proposition 2 (rank-deficient channel). *If the forward or backward channel is rank- k , then regardless of the RIS size and architecture, the n -th singular value of the equivalent channel is bounded by*

$$\sigma_n(\mathbf{H}) \leq \sigma_{n-k}(\mathbf{T}), \quad \text{if } n > k, \quad (3.15)$$

$$\sigma_n(\mathbf{H}) \geq \sigma_n(\mathbf{T}), \quad \text{if } n < N - k + 1, \quad (3.16)$$

where

$$\mathbf{T}\mathbf{T}^H = \begin{cases} \mathbf{H}_D(\mathbf{I} - \mathbf{V}_F\mathbf{V}_F^H)\mathbf{H}_D^H, & \text{if } \text{rank}(\mathbf{H}_F) = k, \\ \mathbf{H}_D^H(\mathbf{I} - \mathbf{U}_B\mathbf{U}_B^H)\mathbf{H}_D, & \text{if } \text{rank}(\mathbf{H}_B) = k, \end{cases} \quad (3.17)$$

and \mathbf{V}_F and \mathbf{U}_B are the right and left compact singular matrices of \mathbf{H}_F and \mathbf{H}_B , respectively.

Proof. Please refer to Appendix 4.1.3. \square

Corollary 2.1 (extreme singular values). *With a sufficiently large RIS, the first k channel singular values are unbounded above while the last k channel singular values can be suppressed to zero.*

Corollary 2.2 (LoS channel⁴). *If the forward or backward channel is LoS, then a RIS can at most enlarge (resp. suppress) the n -th ($n \geq 2$) channel singular value to the $(n - 1)$ -th (resp. n -th) singular value of \mathbf{T} , that is,*

$$\sigma_1(\mathbf{H}) \geq \sigma_1(\mathbf{T}) \geq \sigma_2(\mathbf{H}) \geq \dots \geq \sigma_{N-1}(\mathbf{T}) \geq \sigma_N(\mathbf{H}) \geq \sigma_N(\mathbf{T}). \quad (3.18)$$

In Section 3.6, we will show by simulation that a finite-size BD-RIS can approach those bounds better than diagonal RIS.

Proposition 3 (fully-connected RIS without direct link). *If the BD-RIS is fully-connected and the direct link is absent, then the channel singular values can be manipulated up to*

$$\text{sv}(\mathbf{H}) = \text{sv}(\mathbf{B}\mathbf{F}), \quad (3.19)$$

where \mathbf{B} and \mathbf{F} are arbitrary matrices with the same singular values as \mathbf{H}_B and \mathbf{H}_F , respectively,

Proof. Please refer to Appendix 4.1.4. \square

The problem now becomes how the singular values of matrix product are bounded by the singular values of its individual factors. Let $N' = \max(N_T, N_S, N_R)$ and $\sigma_n(\mathbf{H}) = \sigma_n(\mathbf{H}_F) = \sigma_n(\mathbf{H}_B) = 0$ for $N < n \leq N'$. We have the following corollaries.

Corollary 3.1 (generic singular value bounds [138]).

$$\prod_{k \in K} \sigma_k(\mathbf{H}) \leq \prod_{i \in I} \sigma_i(\mathbf{H}_B) \prod_{j \in J} \sigma_j(\mathbf{H}_F), \quad (3.20)$$

⁴A similar result has been derived for diagonal RIS in [137].

for all admissible triples $(I, J, K) \in T_r^{N'}$ with $r < N'$, where

$$\begin{aligned} T_r^{N'} &\triangleq \left\{ (I, J, K) \in U_r^{N'} \mid \forall p < r, (F, G, H) \in T_p^r, \right. \\ &\quad \left. \sum_{f \in F} i_f + \sum_{g \in G} j_g \leq \sum_{h \in H} k_h + p(p+1)/2 \right\}, \\ U_r^{N'} &\triangleq \left\{ (I, J, K) \mid \sum_{i \in I} i + \sum_{j \in J} j = \sum_{k \in K} k + r(r+1)/2 \right\}. \end{aligned}$$

Corollary 3.2 (upper bound on the largest singular value).

$$\sigma_1(\mathbf{H}) \leq \sigma_1(\mathbf{H}_B) \sigma_1(\mathbf{H}_F). \quad (3.21)$$

Corollary 3.3 (upper bound on the product of first k singular values).

$$\prod_{n=1}^k \sigma_n(\mathbf{H}) \leq \prod_{n=1}^k \sigma_n(\mathbf{H}_B) \prod_{n=1}^k \sigma_n(\mathbf{H}_F). \quad (3.22)$$

Corollary 3.4 (upper bound on the sum of first k singular values to the power of p).

$$\sum_{n=1}^k \sigma_n^p(\mathbf{H}) \leq \sum_{n=1}^k \sigma_n^p(\mathbf{H}_B) \sigma_n^p(\mathbf{H}_F), \quad p > 0. \quad (3.23)$$

When $k = N'$ and $p = 2$, (3.23) suggests the channel power is upper bounded by the sum of (sorted) element-wise power product of backward and forward subchannels.

Tight bounds are inapplicable when a MIMO direct link is present, as the RIS needs to balance the direct-indirect (additive) and backward-forward (multiplicative) subspace alignments. Such a balance often involves optimization approaches and another example will be discussed in Section 3.4.2.

3.4 Achievable Rate Maximization

The MIMO achievable rate maximization problem is formulated w.r.t. joint active and passive beamforming

$$\max_{\mathbf{W}, \Theta} R = \log \det \left(\mathbf{I} + \frac{\mathbf{W}^H \mathbf{H}^H \mathbf{H} \mathbf{W}}{\eta} \right) \quad (3.24a)$$

$$\text{s.t.} \quad \|\mathbf{W}\|_F^2 \leq P, \quad (3.24b)$$

$$\Theta_g^H \Theta_g = \mathbf{I}, \quad \forall g, \quad (3.24c)$$

where \mathbf{W} is the transmit precoder, R is the achievable rate, η is the noise power, and P is the transmit power budget. Two methods are proposed below to solve problem (3.24).

3.4.1 Alternating Optimization

Consider an AO approach that updates Θ and \mathbf{W} iteratively. For a given \mathbf{W} , the passive beamforming subproblem is

$$\max_{\Theta} \log \det \left(\mathbf{I} + \frac{\mathbf{H} \mathbf{Q} \mathbf{H}^H}{\eta} \right) \quad (3.25a)$$

$$\text{s.t.} \quad \Theta_g^H \Theta_g = \mathbf{I}, \quad \forall g, \quad (3.25b)$$

where $\mathbf{Q} \triangleq \mathbf{W} \mathbf{W}^H$ is the transmit covariance matrix.

Lemma 2. *The Euclidean gradient of (3.25a) w.r.t. BD-RIS block g is*

$$\frac{\partial R}{\partial \Theta_g^*} = \frac{1}{\eta} \mathbf{H}_{B,g}^H \left(\mathbf{I} + \frac{\mathbf{H} \mathbf{Q} \mathbf{H}^H}{\eta} \right)^{-1} \mathbf{H} \mathbf{Q} \mathbf{H}_{F,g}^H. \quad (3.26)$$

Proof. Please refer to Appendix 4.1.5. □

Algorithm 1 is then invoked to solve problem (3.24) where line 4 uses (3.26) explicitly. Since (3.25a) is a concave function of Θ , convergence to local-optimal points is guaranteed. On the other hand, the global optimal transmit precoder for a fixed Θ is given by the eigenmode transmission [139]

$$\mathbf{W}^* = \mathbf{V} \mathbf{S}^{*1/2}, \quad (3.27)$$

where \mathbf{V} is the right channel singular matrix and \mathbf{S}^* is the optimal water-filling power allocation matrix. The overall AO algorithm converges to local-optimal points of problem (3.24) since each subproblem is solved optimally and the objective is bounded above.

3.4.2 Low-Complexity Solution

We then propose a low-complexity solution to problem (3.24) based on channel shaping. The passive beamforming subproblem (3.25) involves transmit covariance matrix \mathbf{Q} and thus requires iterative RCG update. Instead, we decouple the joint RIS-transceiver design by recasting (3.25) as channel power maximization

$$\max_{\Theta} \quad \|\mathbf{H}_D + \mathbf{H}_B \Theta \mathbf{H}_F\|_F^2 \quad (3.28a)$$

$$\text{s.t.} \quad \Theta_g^H \Theta_g = \mathbf{I}, \quad \forall g. \quad (3.28b)$$

Remark 3. As mentioned in Section 3.3.3, the key of solving (3.28) is to balance the additive and multiplicative subspace alignments. Problem (3.28) is very similar (in terms of maximizing the inner product of \mathbf{H}_D and $\mathbf{H}_B \Theta \mathbf{H}_F$) to the weighted orthogonal Procrustes problem [140]

$$\min_{\Theta} \quad \|\mathbf{H}_D - \mathbf{H}_B \Theta \mathbf{H}_F\|_F^2 \quad (3.29a)$$

$$\text{s.t.} \quad \Theta^H \Theta = \mathbf{I}, \quad (3.29b)$$

which has no trivial solution. One lossy transformation, by moving Θ to one side [141], formulates standard orthogonal Procrustes problems

$$\min_{\Theta} \quad \|\mathbf{H}_B^\dagger \mathbf{H}_D - \Theta \mathbf{H}_F\|_F^2 \text{ or } \|\mathbf{H}_D \mathbf{H}_F^\dagger - \mathbf{H}_B \Theta\|_F^2 \quad (3.30a)$$

$$\text{s.t.} \quad \Theta^H \Theta = \mathbf{I}, \quad (3.30b)$$

which has global optimal solutions

$$\Theta^* = \mathbf{U} \mathbf{V}^H \quad (3.31)$$

where \mathbf{U} and \mathbf{V} are the left and right singular matrices of $\mathbf{H}_B^\dagger \mathbf{H}_D \mathbf{H}_F^H$ or $\mathbf{H}_B^H \mathbf{H}_D \mathbf{H}_F^\dagger$ [142]. This suboptimal solution only applies to fully-connected BD-RIS.

Inspired by [143], we propose a general solution to problem (3.28) with arbitrary group size. The idea is to successively approximate the quadratic objective (3.28a) by local Taylor expansions and solve each step in closed form.

Proposition 4. Starting from any $\Theta^{(0)} \in \mathbb{U}^{N_S \times N_S}$, the sequence

$$\Theta_g^{(r+1)} = \mathbf{U}_g^{(r)} \mathbf{V}_g^{(r)}, \quad \forall g. \quad (3.32)$$

converges to a stationary point of (3.28), where $\mathbf{U}_g^{(r)}$ and $\mathbf{V}_g^{(r)}$ are the left and right compact singular matrix of

$$\mathbf{M}_g^{(r)} = \mathbf{H}_{B,g}^H \left(\mathbf{H}_D + \mathbf{H}_B \text{diag}(\boldsymbol{\Theta}_{[1:g-1]}^{(r+1)}, \boldsymbol{\Theta}_{[g:G]}^{(r)}) \mathbf{H}_F \right) \mathbf{H}_{F,g}^H \quad (3.33)$$

Proof. Please refer to Appendix 4.1.6. \square

Once the channel shaping problem (3.28) is solved, the transmit precoder can be obtained by (3.27). This two-stage approach decouples both blocks and is computationally efficient.

3.5 MIMO-IC

3.5.1 Leakage Interference Minimization

$$\min_{\boldsymbol{\Theta}, \{\mathbf{G}_k\}, \{\mathbf{W}_k\}} \sum_{j \neq k} \sum \left\| \mathbf{G}_k (\mathbf{H}_{kj}^D + \mathbf{H}_k^B \boldsymbol{\Theta} \mathbf{H}_j^F) \mathbf{W}_j \right\|_F^2 \quad (3.34a)$$

$$\text{s.t.} \quad \boldsymbol{\Theta}_g^H \boldsymbol{\Theta}_g = \mathbf{I}, \quad \forall g, \quad (3.34b)$$

$$\mathbf{G}_k \mathbf{G}_k^H = \mathbf{I}, \quad \mathbf{W}_k^H \mathbf{W}_k = \mathbf{I}, \quad \forall k. \quad (3.34c)$$

The non-convex problem can be solved by Block Coordinate Descent (BCD) method. For a given $\boldsymbol{\Theta}$, it reduces to conventional linear beamforming problem, for which an iterative algorithm alternating between the original and reciprocal networks is proposed in [144, 139]. At iteration r , the combiner at receiver k is updated as

$$\mathbf{G}_k^{(r)} = \mathbf{U}_{k,N}^{(r-1)H}, \quad (3.35)$$

where $\mathbf{U}_{k,N}^{(r-1)}$ is the eigenvectors corresponding to N smallest eigenvalues of interference covariance matrix $\mathbf{Q}_k^{(r-1)} = \sum_{j \neq k} \mathbf{H}_{kj} \mathbf{W}_j^{(r-1)} \mathbf{W}_j^{(r-1)H} \mathbf{H}_{kj}^H$. The precoder at transmitter j is updated as

$$\mathbf{W}_j^{(r)} = \bar{\mathbf{U}}_{j,N}^{(r)}, \quad (3.36)$$

where $\bar{\mathbf{U}}_{j,N}^{(r)}$ corresponds to interference covariance matrix $\bar{\mathbf{Q}}_j^{(r)} = \sum_{k \neq j} \mathbf{H}_{kj}^H \mathbf{G}_k^{(r)H} \mathbf{G}_k^{(r)} \mathbf{H}_{kj}$ in the reciprocal network. Once $\{\mathbf{G}_k\}$ and $\{\mathbf{W}_k\}$ are determined, we define $\bar{\mathbf{H}}_{kj}^D \triangleq \mathbf{G}_k \mathbf{H}_{kj}^D \mathbf{W}_j$,

$\bar{\mathbf{H}}_k^B \triangleq \mathbf{G}_k \mathbf{H}_k^B$, and $\bar{\mathbf{H}}_j^F \triangleq \mathbf{H}_j^F \mathbf{W}_j$. The BD RIS subproblem reduces to

$$\min_{\boldsymbol{\Theta}} \sum_{j \neq k} \sum \left\| (\bar{\mathbf{H}}_{kj}^D + \bar{\mathbf{H}}_k^B \boldsymbol{\Theta} \bar{\mathbf{H}}_j^F) \right\|_F^2 \quad (3.37a)$$

$$\text{s.t.} \quad \boldsymbol{\Theta}_g^H \boldsymbol{\Theta}_g = \mathbf{I}, \quad \forall g. \quad (3.37b)$$

Proposition 5. *Start from any $\boldsymbol{\Theta}^{(0)}$, the sequence*

$$\boldsymbol{\Theta}_g^{(r+1)} = \mathbf{U}_g^{(r)} \mathbf{V}_g^{(r)}, \quad \forall g \quad (3.38)$$

converges to a stationary point of (3.37), where $\mathbf{U}_g^{(r)}$ and $\mathbf{V}_g^{(r)}$ are left and right singular matrix of

$$\mathbf{M}_g^{(r)} = \sum_{j \neq k} (\mathbf{B}_{k,g} \boldsymbol{\Theta}_g^{(r)} \mathbf{H}_{j,g}^F - \mathbf{H}_{k,g}^B \mathbf{H}_{k,j,g}^D) \mathbf{H}_{j,g}^F \mathbf{H}_{j,g}^H, \quad (3.39)$$

where $\mathbf{B}_{k,g} = \lambda_1(\mathbf{H}_{k,g}^B \mathbf{H}_{k,g}^B \mathbf{H}_{k,g}^H) \mathbf{I} - \mathbf{H}_{k,g}^B \mathbf{H}_{k,g}^B \mathbf{H}_{k,g}^H$ and

$$\mathbf{D}_{k,j,g}^{(r)} = \mathbf{H}_{jk}^D + \sum_{g' < g} \mathbf{H}_{k,g'}^B \mathbf{H}_{g'} \boldsymbol{\Theta}_{g'}^{(r+1)} \mathbf{H}_{k,g'}^F + \sum_{g' > g} \mathbf{H}_{k,g'}^B \mathbf{H}_{g'} \boldsymbol{\Theta}_{g'}^{(r)} \mathbf{H}_{k,g'}^F. \quad (3.40)$$

Proof. To be added. □

Fig. 3.2 illustrates how BD RIS helps to reduce the leakage interference. In this case, a fully-connected 2^n -element BD RIS is almost as good as a diagonal 2^{n+2} -element RIS in terms of leakage interference. Interestingly, the result suggests that BD RIS can achieve a higher DoF than diagonal RIS in MIMO-IC, which is not the case in MIMO-PC (as discussed in ??).

3.5.2 Weighted Sum-Rate Maximization

$$\max_{\boldsymbol{\Theta}, \{\mathbf{W}_k\}} J_2 = \sum_k \rho_k \log \det \left(\mathbf{I} + \mathbf{W}_k \mathbf{H}_{kj}^H \mathbf{Q}_k^{-1} \mathbf{H}_{kj} \mathbf{W}_k \right) \quad (3.41a)$$

$$\text{s.t.} \quad \boldsymbol{\Theta}_g^H \boldsymbol{\Theta}_g = \mathbf{I}, \quad \forall g, \quad (3.41b)$$

$$\|\mathbf{W}_k\|_F^2 \leq P_k, \quad \forall k \quad (3.41c)$$

where ρ_k is the weight of user k and \mathbf{Q}_k is the interference-plus-noise covariance matrix

$$\mathbf{Q}_k = \sum_{j \neq k} \mathbf{H}_{kj} \mathbf{W}_j \mathbf{W}_j^H \mathbf{H}_{kj}^H + \eta \mathbf{I}. \quad (3.42)$$

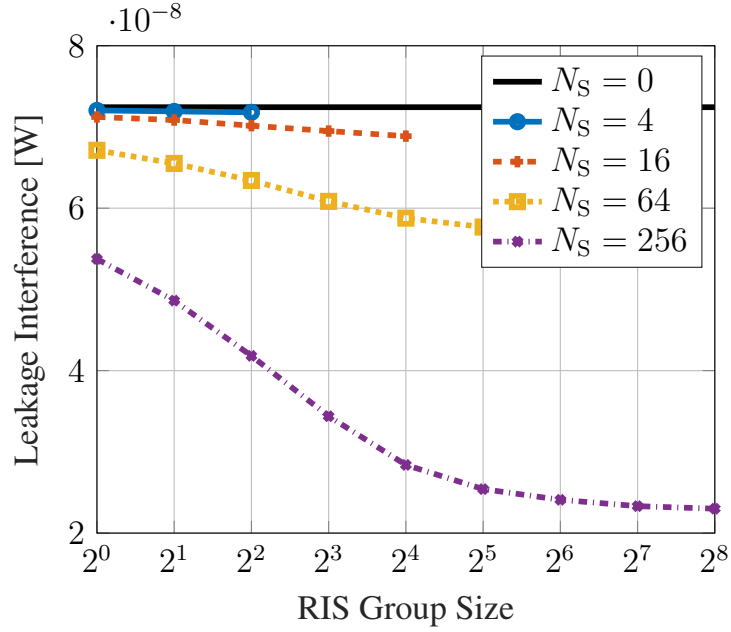


Fig. 3.2 Average leakage interference versus RIS elements N^S and group size L . Transmitters and receivers are randomly generated in a disk of radius 50 m centered at the RIS. $(N^T, N^R, N^E, K) = (8, 4, 3, 5)$, $(\gamma^D, \gamma^F, \gamma^B) = (3, 2.4, 2.4)$, and reference pathloss at 1 m is -30 dB.

For a given Θ , (3.41) reduces to conventional linear beamforming problem, for which a closed-form iterative solution based on mutual information-Minimum Mean-Square-Error (MMSE) relationship is proposed in [145]. At iteration r , the MMSE combiner at receiver k is

$$\mathbf{G}_k^{(r)} = \mathbf{W}_k^{(r-1)\text{H}} \mathbf{H}_{kk}^{\text{H}} (\mathbf{Q}_k^{(r-1)} + \mathbf{H}_{kk} \mathbf{W}_k^{(r-1)} \mathbf{W}_k^{(r-1)\text{H}} \mathbf{H}_{kk}^{\text{H}})^{-1}, \quad (3.43)$$

the corresponding error matrix is

$$\mathbf{E}_k^{(r)} = (\mathbf{I} + \mathbf{W}_k^{(r-1)\text{H}} \mathbf{H}_{kk}^{\text{H}} \mathbf{Q}_k^{(r-1)} \mathbf{H}_{kk} \mathbf{W}_k^{(r-1)})^{-1}, \quad (3.44)$$

the Mean-Square Error (MSE) weight is

$$\boldsymbol{\Omega}_k^{(r)} = \rho_k \mathbf{E}_k^{(r)-1}, \quad (3.45)$$

the Lagrange multiplier is

$$\lambda_k^{(r)} = \frac{\text{tr}(\eta \boldsymbol{\Omega}_k^{(r)} \mathbf{G}_k^{(r)} \mathbf{G}_k^{(r)\text{H}} + \sum_j \boldsymbol{\Omega}_k^{(r)} \mathbf{T}_{kj}^{(r)} \mathbf{T}_{kj}^{(r)\text{H}} - \boldsymbol{\Omega}_j^{(r)} \mathbf{T}_{jk}^{(r)} \mathbf{T}_{jk}^{(r)\text{H}})}{P_k}, \quad (3.46)$$

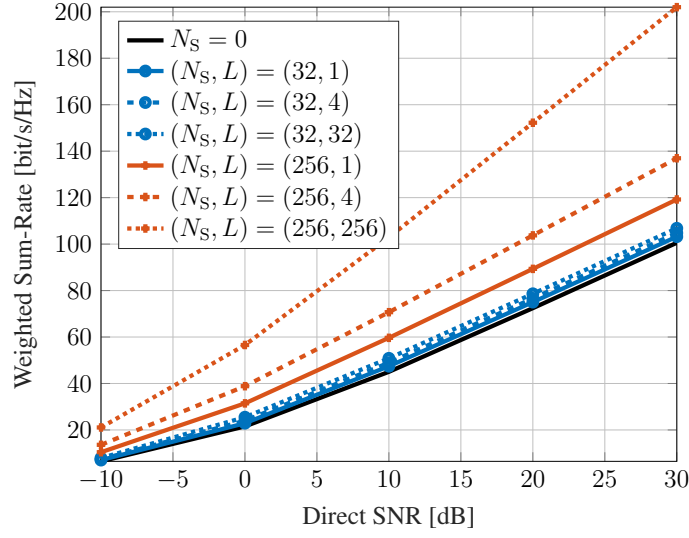


Fig. 3.3 Average weighted sum-rate versus SNR, RIS elements N^S and group size L . $(N^T, N^R, N^E, K) = (8, 4, 3, 5)$, $(\Lambda^D, \Lambda^F, \Lambda^B) = (65, 54, 46)$ dB, $\rho_k = 1$, $\forall k$.

where $\mathbf{T}_{kj}^{(r)} = \mathbf{G}_k^{(r)} \mathbf{H}_{kj} \mathbf{W}_j^{(r)}$. The precoder at transmitter k is

$$\mathbf{W}_k^{(r)} = \left(\sum_j \mathbf{H}_{jk}^H \mathbf{G}_j^{(r)H} \mathbf{\Omega}_k^{(r)} \mathbf{G}_j^{(r)} \mathbf{H}_{jk} + \lambda_k^{(r)} \mathbf{I} \right)^{-1} \mathbf{H}_{kk}^H \mathbf{G}_j^{(r)H} \mathbf{\Omega}_k^{(r)}. \quad (3.47)$$

Once $\{\mathbf{W}_k\}$ is determined, the complex derivative of (3.41a) w.r.t. RIS block g is

$$\begin{aligned} \frac{\partial J_2}{\partial \Theta_g^*} &= \sum_k \rho_k \mathbf{H}_{k,g}^B{}^H \mathbf{Q}_k^{-1} \mathbf{H}_{kk} \mathbf{W}_k \mathbf{E}_k \mathbf{W}_k^H \\ &\quad \times \left(\mathbf{H}_{k,g}^F{}^H - \mathbf{H}_{kk}^H \mathbf{Q}_k^{-1} \sum_{j \neq k} \mathbf{H}_{kj} \mathbf{W}_j \mathbf{W}_j^H \mathbf{H}_{j,g}^F{}^H \right). \end{aligned} \quad (3.48)$$

The RIS subproblem can be solved by RCG Algorithm ?? with (??) replaced by (3.48).

A new observation from Fig. 3.3 that the interference alignment capability of BD RIS scales much faster with group size than number of elements.⁵

3.6 Simulation Results

In this section, we provide numerical results to evaluate the proposed BD-RIS designs. Consider a distance-dependent path loss model $\Lambda(d) = \Lambda_0 d^{-\gamma}$ where Λ_0 is the reference path loss at distance 1 m, d is the propagation distance, and γ is the path loss exponent. The

⁵The results are not very stable and depend heavily on initialization.

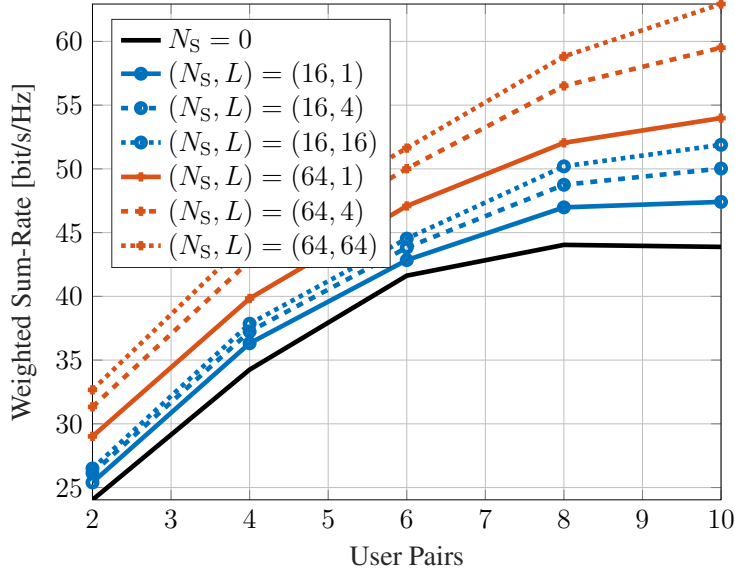


Fig. 3.4 Average weighted sum-rate versus user pairs K , RIS elements N^S and group size L at SNR = 15 dB. $(N^T, N^R, N^E) = (4, 4, 3)$, $\rho_k = 1$, $\forall k$.

Table 3.1 Average Performance of BD-RIS Designs

RCG path	$N_S = 16$			$N_S = 256$		
	Objective	Iterations	Time [s]	Objective	Iterations	Time [s]
Geodesic	4.355×10^{-3}	11.61	2.038×10^{-2}	1.164×10^{-2}	25.78	3.216
Non-geodesic	4.168×10^{-3}	169.5	1.420×10^{-1}	8.873×10^{-3}	278.1	27.81

small-scale fading model is $\mathbf{H} = \sqrt{\kappa/(1+\kappa)}\mathbf{H}_{\text{LoS}} + \sqrt{1/(1+\kappa)}\mathbf{H}_{\text{NLoS}}$, where κ is the Rician K -factor, \mathbf{H}_{LoS} is the deterministic LoS component, and $\mathbf{H}_{\text{NLoS}} \sim \mathcal{CN}(\mathbf{0}, \mathbf{I})$ is the Rayleigh component. We set $\Lambda_0 = -30$ dB, $d_D = 14.7$ m, $d_F = 10$ m, $d_B = 6.3$ m, $\gamma_D = 3$, $\gamma_F = 2.4$ and $\gamma_B = 2$ for reference, which corresponds to a typical indoor environment with $\Lambda_D = -65$ dB, $\Lambda_F = -54$ dB, $\Lambda_B = -46$ dB. The indirect path via RIS is thus 35 dB weaker than the direct path. $\kappa \rightarrow \infty$ is assumed for all channels unless otherwise specified.

3.6.1 Channel Singular Values Redistribution

3.6.1.1 Pareto Frontier

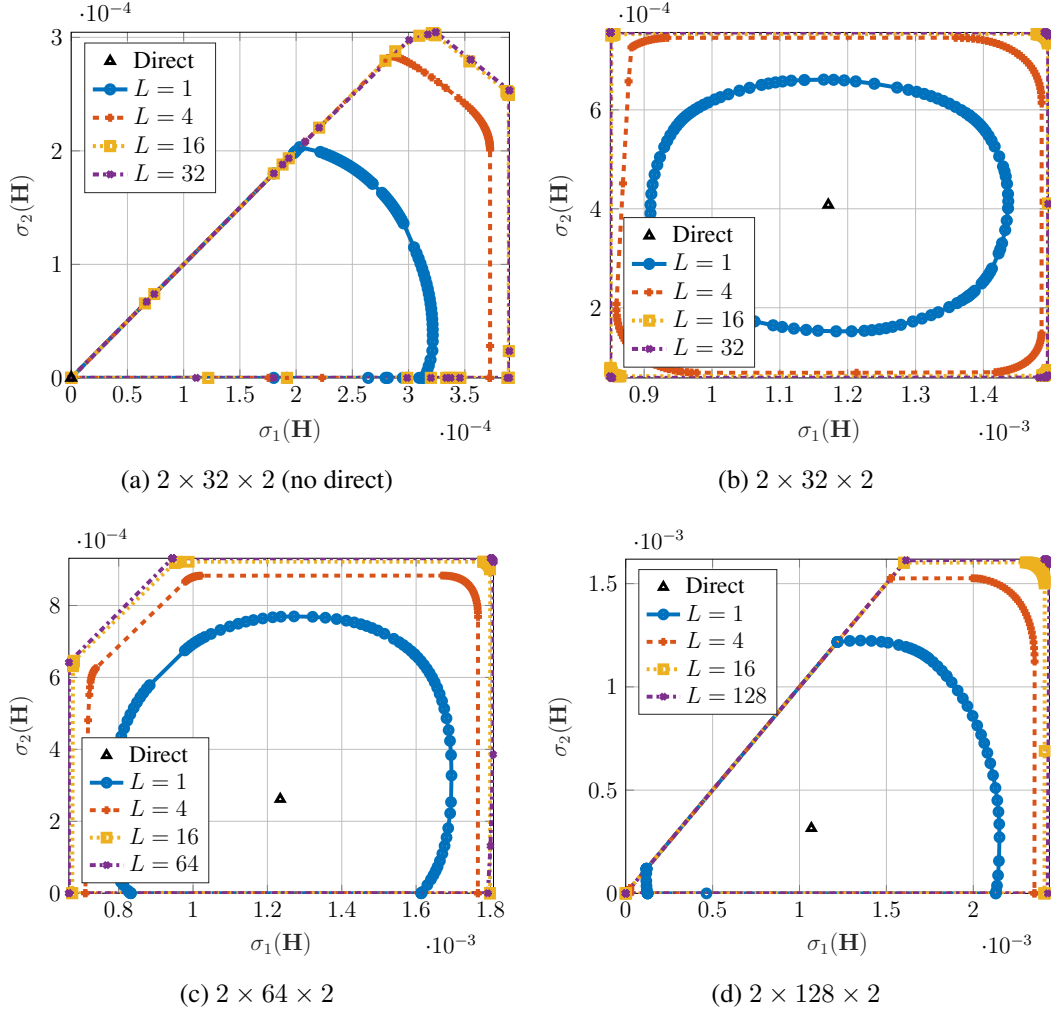


Fig. 3.5 Pareto frontiers of singular values of a 2T2R channel reshaped by a RIS.

Fig. 3.5 shows the Pareto singular values of a 2T2R MIMO reshaped by a RIS. When the direct link is absent, the achievable regions in Fig. 3.5(a) are shaped like pizza slices. This is because $\sigma_1(\mathbf{H}) \geq \sigma_2(\mathbf{H}) \geq 0$ and there exists a trade-off between aligning the two subspaces. We observe that the smallest singular value is enhanced up to 2×10^{-4} by diagonal RIS and 3×10^{-4} by fully-connected BD-RIS, corresponding to a 50% gain. When the direct link is present, the shape of the singular value region depends heavily on the relative strength of the indirect link. In Fig. 3.5(b), a 32-element RIS is insufficient to compensate the 35 dB path loss imbalance and results in a limited singular value region that is symmetric around the

direct point. As the group size L increases, the shape of the region evolves from elliptical to square. This transformation not only provides a better trade-off in subchannel manipulation but also improves the dynamic range of $\sigma_1(\mathbf{H})$ and $\sigma_2(\mathbf{H})$ by 22 % and 38 %, respectively. The achievable singular value region also enlarges as the number of scattering elements N_S increases. In particular, Fig. 3.5(d) shows that the equivalent channel can be completely nulled by a 128-element BD-RIS but not by a diagonal one. Those results demonstrate the superior channel shaping capability of BD-RIS for better signal enhancement and interference suppression.

3.6.1.2 Analytical Bounds and Numerical Results

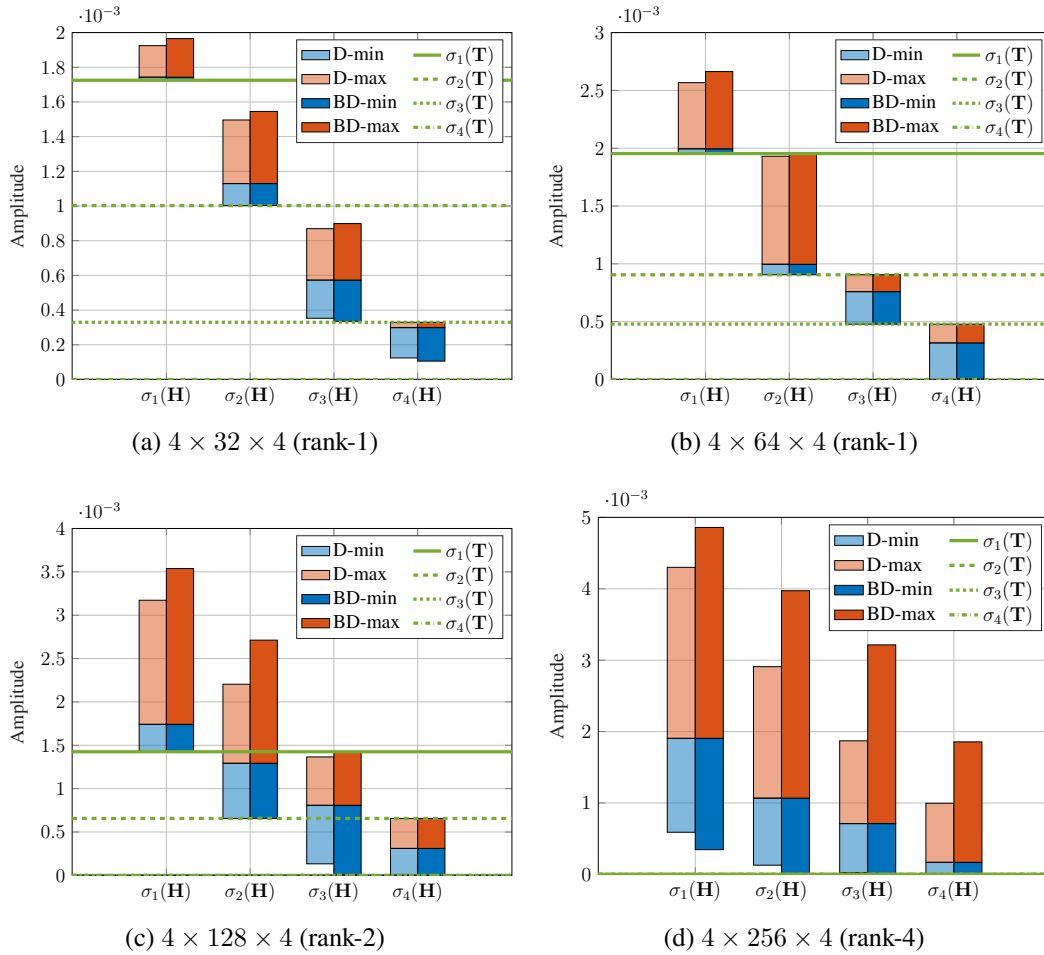


Fig. 3.6 Achievable channel singular values: analytical bounds (green lines) and numerical optimization results (blue and red bars). ‘D’ means diagonal RIS and ‘BD’ means fully-connected BD-RIS. ‘rank- k ’ refers to the forward channel.

Fig. 3.6 illustrates the analytical singular value bounds in Proposition 2 and the numerical results obtained by solving problem (3.7) with $\rho_n = \pm 1$ and $\rho_{n'} = 0, \forall n' \neq n$. Here we assume a rank- k forward channel without loss of generality. When the RIS is in the vicinity of the transmitter, Figs. 3.6(a) and 3.6(b) show that the achievable channel singular values indeed satisfy Corollary 2.2, namely $\sigma_1(\mathbf{H}) \geq \sigma_1(\mathbf{T})$, $\sigma_2(\mathbf{T}) \leq \sigma_2(\mathbf{H}) \leq \sigma_1(\mathbf{T})$, etc. It is obvious that BD-RIS can approach those bounds better than diagonal RIS especially for a small N_S . Another example is given in Fig. 3.6(c) with rank-2 forward channel. The first two channel singular values are unbounded above and bounded below by the first two singular values of \mathbf{T} , while the last two singular values can be suppressed to zero and bounded above by the first two singular values of \mathbf{T} . Those observations align with Proposition 2 and Corollary 2.1. Finally, Fig. 3.6(d) confirms there are no extra singular value bounds when both forward and backward channels are full-rank. This can be predicted from (3.17) where the compact singular matrix \mathbf{V}_F becomes unitary and $\mathbf{T} = \mathbf{0}$. The numerical results are consistent with the analytical bounds, and we conclude that the channel shaping advantage of BD-RIS over diagonal RIS scales with forward and backward channel ranks.

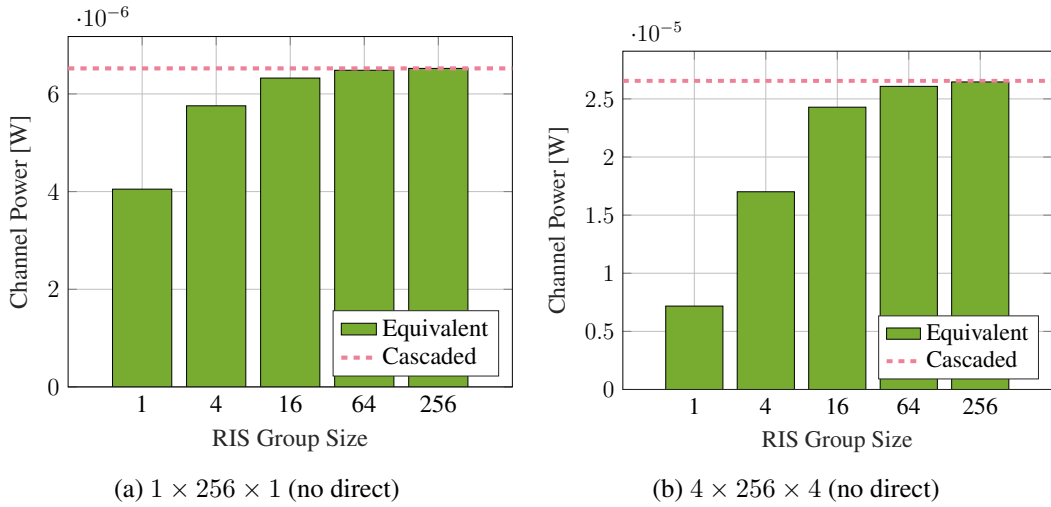


Fig. 3.7 Average maximum channel power versus BD-RIS group size and MIMO dimensions. ‘Cascaded’ refers to the available power of the cascaded channel, i.e., the sum of (sorted) element-wise power product of backward and forward subchannels.

Fig. 3.7 compares the analytical channel power bound in Corollary 3.4 with $k = N'$, $p = 2$ and the numerical results obtained by solving problem (3.28) when the direct link is absent. Here, a fully-connected BD-RIS can attain the upper bound either in closed form or via optimization approach (3.32). For the SISO case in Fig. 3.7(a), the maximum channel power is approximately 4×10^{-6} by diagonal RIS and 6.5×10^{-6} by fully-connected BD-RIS, corresponding to a 62.5% gain. This aligns with the asymptotic BD-RIS scaling law derived

for SISO in [2]. Interestingly, the gain surges to 270 % in 4T4R MIMO as shown in Fig. 3.7(b). This is because subspace alignment boils down to phase matching in SISO such that both triangular and Cauchy-Schwarz inequalities in [2, (50)] can be simultaneously tight regardless of the group size. That is, diagonal RIS is sufficient for subspace alignment in SISO while the 62.5 % gain from BD-RIS comes purely from subchannel rearrangement (i.e., pairing the forward and backward channels from strongest to weakest). Now consider a diagonal RIS in MIMO. Each element can only apply a common phase shift to the associated rank-1 $N_R \times N_T$ indirect channel. Therefore, perfect subspace alignment of indirect channels through different elements is generally impossible. It means the disadvantage of diagonal RIS in subspace alignment and subchannel rearrangement scales with MIMO dimensions. We thus conclude that the power gain of BD-RIS scales with group size and MIMO dimensions.

3.6.2 Achievable Rate Maximization

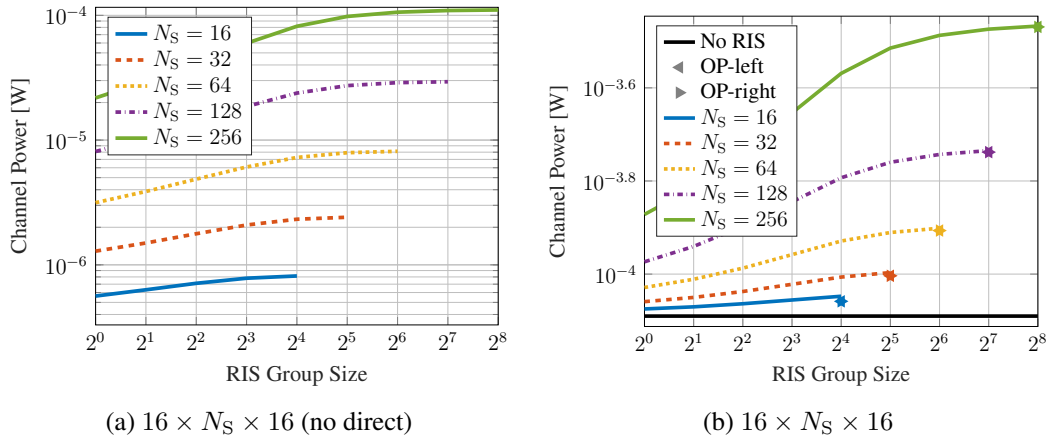


Fig. 3.8 Average maximum channel power versus RIS configuration. ‘OP-left’ and ‘OP-right’ refer to the suboptimal solutions to problem (3.28) by lossy transformation (3.30) where Θ is to the left and right of the product, respectively.

We first focus on channel shaping subproblem (4.9). Fig. 3.8 shows the achievable channel power under different RIS configurations. An interesting observation is that the relative power gain of BD-RIS over diagonal RIS is even larger with direct link. For example, a 64-element fully BD-RIS can almost provide the same channel power as a 256-element diagonal RIS in Fig. 3.8b, but not in Fig. 3.8a. This is because the RIS needs to balance the multiplicative forward-backward combining and the additive direct-indirect combining, such that the subspace alignment advantage of BD-RIS becomes more pronounced. We also notice that the suboptimal solutions (3.31) for fully-connected BD-RIS by lossy transformation (3.30) are very close to optimal especially for a large N_S .

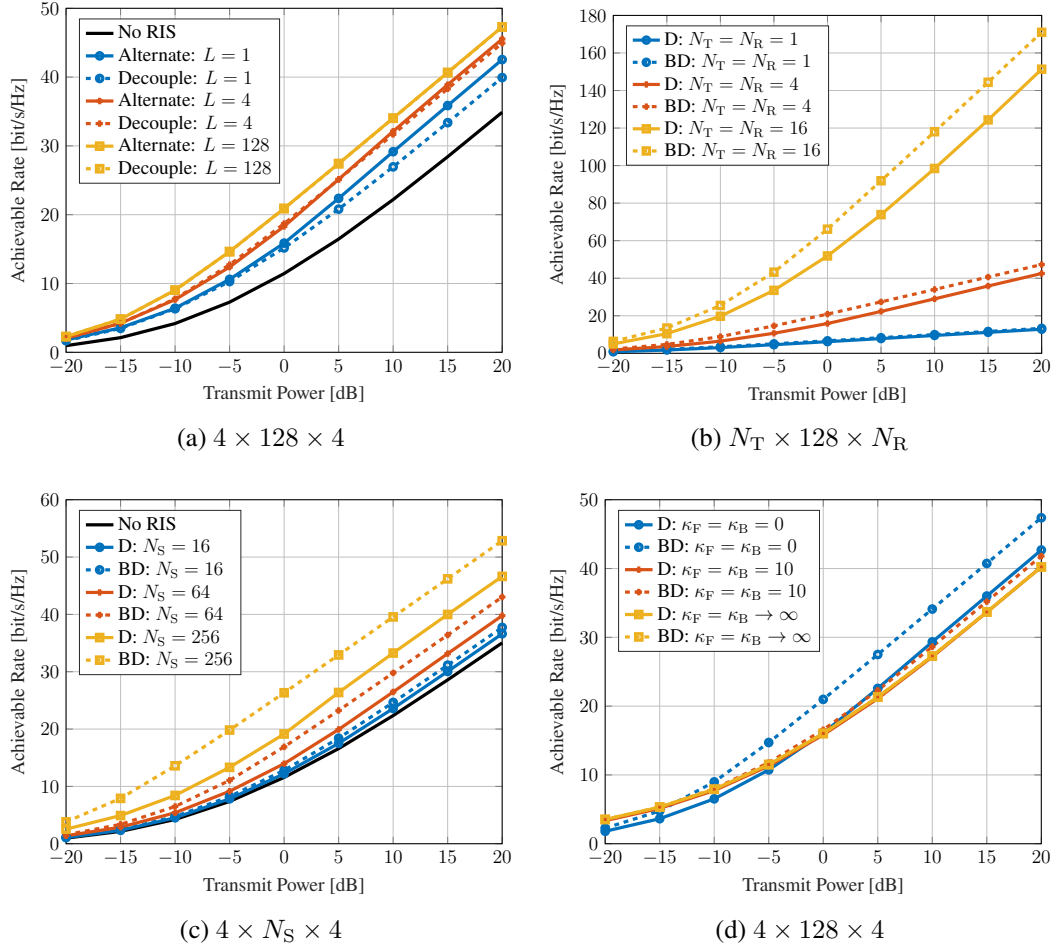


Fig. 3.9 Average achievable rate versus MIMO and RIS configurations. The noise power is $\eta = -75$ dB, corresponding to a direct SNR of -10 to 30 dB. ‘Alternate’ refers to the alternating optimization and ‘Decouple’ refers to the low-complexity design. ‘D’ means diagonal RIS and ‘BD’ means fully-connected BD-RIS.

Fig. 3.9 presents the achievable rate under different MIMO and RIS configurations. At a transmit power of 10 dB, Fig. 3.9(a) shows that introducing a 128 -element diagonal RIS to $4T4R$ MIMO can improve the achievable rate from 22.2 bps/Hz to 29.2 bps/Hz ($+31.5\%$). In contrast, a BD-RIS of group size 4 and 128 can further improve the rate to 32.1 bps/Hz ($+44.6\%$) and 34 bps/Hz ($+53.2\%$), respectively. Interestingly, the gap between the optimal AO approach (3.25)–(3.27) and the low-complexity solution (3.32) and (3.27) narrows as the group size increases, and completely vanishes for a fully-connected BD-RIS. This implies that the RIS-transceiver design can be completely decoupled via channel shaping with marginal performance loss. Figs. 3.9(b) and 3.9(c) also confirm the advantage of BD-RIS grows with the number of transmit, scatter, and receive antennas. In the low power regime (-20 to -10 dB), the slope of the achievable rate is significantly larger with BD-RIS, suggesting

that multiple streams can be activated at a much lower SNR. This is because BD-RIS not only spreads the channel singular values to a wider range, but also provides a better trade-off between subchannels (c.f. Fig. 3.5). Finally, Fig. 3.9(d) shows that the gap between diagonal and BD-RIS narrows as the Rician K -factor increases and becomes indistinguishable in LoS environment. The observation is expected from previous studies [2, 112, 113] and aligns with Corollary 2.2, which suggests that the BD-RIS should be deployed in rich-scattering environments to exploit its channel shaping potential.

3.7 Conclusion

This chapter analyzes the channel shaping capability of RIS in terms of singular values redistribution. We consider a general BD architecture that allows elements within the same group to interact, enabling more sophisticated manipulation than diagonal RIS. This translates to a wider dynamic range (with better trade-off) of singular values and significant power and rate gains, especially in large-scale MIMO systems. We characterize the Pareto frontiers of channel singular values via optimization approach and provide analytical bounds in rank-deficient and fully-connected scenarios. An efficient RCG algorithm is proposed for smooth BD-RIS optimization problems, which offers lower computation complexity and faster convergence than existing methods. We also present two beamforming designs for rate maximization problem, one based on alternating optimization for optimal performance and the other decouples the RIS-transceiver design for lower complexity. Extensive simulations show that the advantage of BD-RIS stems from its superior subspace alignment and subchannel rearrangement capability, which scales with the number of elements, group size, MIMO dimensions, and channel diversity.

One future direction is introducing BD-RIS to MIMO interference channel for interference alignment or cancellation. Another open issue is to exploit different groups of BD-RIS to enhance the channel response (and possibly ride extra information) at different frequencies. Incorporating a RIS at both transmitter and receiver sides provides even stronger manipulation that potentially align both direct-indirect and forward-backward subspaces simultaneously.

Chapter 4

Appendix

4.1 Proofs for Chapter 3

4.1.1 Proof of Lemma 1

Let $\mathbf{H} = \sum_n \mathbf{u}_n \sigma_n \mathbf{v}_n^H$ be the compact SVD of the equivalent channel. Since the singular vectors are orthonormal, the n -th singular value can be expressed as

$$\sigma_n = \mathbf{u}_n^H \mathbf{H} \mathbf{v}_n = \mathbf{u}_n^T \mathbf{H}^* \mathbf{v}_n^*, \quad (4.1)$$

whose differential w.r.t. Θ_g^* is

$$\begin{aligned} \partial \sigma_n &= \partial \mathbf{u}_n^T \underbrace{\mathbf{H}^* \mathbf{v}_n^*}_{\sum_m \mathbf{u}_m^* \sigma_m \mathbf{v}_m^T \mathbf{v}_n} + \mathbf{u}_n^T \cdot \partial \mathbf{H}^* \cdot \mathbf{v}_n^* + \underbrace{\mathbf{u}_n^T \mathbf{H}^*}_{\mathbf{u}_n^T \sum_m \mathbf{u}_m^* \sigma_m \mathbf{v}_m^T} \partial \mathbf{v}_n^* \\ &= \underbrace{\partial \mathbf{u}_n^T \mathbf{u}_n^*}_{\partial 1=0} \cdot \sigma_n + \mathbf{u}_n^T \cdot \partial \mathbf{H}^* \cdot \mathbf{v}_n^* + \sigma_n \cdot \underbrace{\mathbf{v}_n^T \partial \mathbf{v}_n^*}_{\partial 1=0} \\ &= \mathbf{u}_n^T \mathbf{H}_{B,g}^* \cdot \partial \Theta_g^* \cdot \mathbf{H}_{F,g}^* \mathbf{v}_n^* \\ &= \text{tr}(\mathbf{H}_{F,g}^* \mathbf{v}_n^* \mathbf{u}_n^T \mathbf{H}_{B,g}^* \cdot \partial \Theta_g^*). \end{aligned}$$

According to [146], the corresponding complex derivative is

$$\frac{\partial \sigma_n}{\partial \Theta_g^*} = \mathbf{H}_{B,g}^H \mathbf{u}_n \mathbf{v}_n^H \mathbf{H}_{F,g}^H. \quad (4.2)$$

A linear combination of (4.2) yields (3.14).

4.1.2 Proof of Proposition 1

The scattering matrix of BD-RIS can be decomposed as¹

$$\Theta = \mathbf{L}\Theta_D\mathbf{R}^H, \quad (4.3)$$

where $\Theta_D \in \mathbb{U}^{N_S \times N_S}$ corresponds to diagonal RIS and $\mathbf{L}, \mathbf{R} \in \mathbb{U}^{N_S \times N_S}$ are block diagonal matrices of $L \times L$ unitary blocks. Manipulating \mathbf{L} and \mathbf{R} rotates the linear spans of $\bar{\mathbf{H}}_B \triangleq \mathbf{H}_B\mathbf{L}$ and $\bar{\mathbf{H}}_F \triangleq \mathbf{R}^H\mathbf{H}_F$ and maintains their rank. On the other hand, there exists a Θ_D such that

$$\begin{aligned} \text{rank}(\mathbf{H}_B\Theta_D\mathbf{H}_F) &= \min(\text{rank}(\mathbf{H}_B), \text{rank}(\Theta_D), \text{rank}(\mathbf{H}_F)) \\ &= \min(\text{rank}(\bar{\mathbf{H}}_B), N_S, \text{rank}(\bar{\mathbf{H}}_F)) \\ &= \max_{\Theta} \text{rank}(\mathbf{H}_B\Theta\mathbf{H}_F) \end{aligned}$$

The same result holds if the direct link is present.

4.1.3 Proof of Proposition 2

We consider rank- k forward channel and the proof follows similarly for rank- k backward channel. Let $\mathbf{H}_F = \mathbf{U}_F\mathbf{\Sigma}_F\mathbf{V}_F^H$ be the compact SVD of the forward channel. The channel Gram matrix $\mathbf{G} \triangleq \mathbf{H}\mathbf{H}^H$ can be written as

$$\begin{aligned} \mathbf{G} &= \mathbf{H}_D\mathbf{H}_D^H + \mathbf{H}_B\Theta\mathbf{U}_F\mathbf{\Sigma}_F\mathbf{\Sigma}_F^H\mathbf{U}_F^H\Theta^H\mathbf{H}_B^H \\ &\quad + \mathbf{H}_B\Theta\mathbf{U}_F\mathbf{\Sigma}_F\mathbf{V}_F^H\mathbf{H}_D^H + \mathbf{H}_D\mathbf{V}_F\mathbf{\Sigma}_F\mathbf{U}_F^H\Theta^H\mathbf{H}_B^H \\ &= \mathbf{H}_D(\mathbf{I} - \mathbf{V}_F\mathbf{V}_F^H)\mathbf{H}_D^H \\ &\quad + (\mathbf{H}_B\Theta\mathbf{U}_F\mathbf{\Sigma}_F + \mathbf{H}_D\mathbf{V}_F)(\mathbf{\Sigma}_F\mathbf{U}_F^H\Theta^H\mathbf{H}_B^H + \mathbf{V}_F^H\mathbf{H}_D^H) \\ &= \mathbf{Y} + \mathbf{Z}\mathbf{Z}^H, \end{aligned}$$

where we define $\mathbf{Y} \triangleq \mathbf{H}_D(\mathbf{I} - \mathbf{V}_F\mathbf{V}_F^H)\mathbf{H}_D^H \in \mathbb{H}^{N_R \times N_R}$ and $\mathbf{Z} \triangleq \mathbf{H}_B\Theta\mathbf{U}_F\mathbf{\Sigma}_F + \mathbf{H}_D\mathbf{V}_F \in \mathbb{C}^{N_R \times k}$. That is to say, \mathbf{G} can be expressed as a Hermitian matrix plus k rank-1 perturbations. According to the Cauchy interlacing formula [142], the n -th eigenvalue of \mathbf{G} is bounded by

$$\lambda_n(\mathbf{G}) \leq \lambda_{n-k}(\mathbf{Y}), \quad \text{if } n > k, \quad (4.4)$$

$$\lambda_n(\mathbf{G}) \geq \lambda_n(\mathbf{Y}), \quad \text{if } n < N - k + 1. \quad (4.5)$$

¹This is because (block) unitary matrices are closed under multiplication.

Since $\mathbf{Y} = \mathbf{T}\mathbf{T}^H$ is positive semi-definite, taking the square roots of (4.4) and (4.5) gives (3.15) and (3.16).

4.1.4 Proof of Proposition 3

Let $\mathbf{H}_B = \mathbf{U}_B \Sigma_B \mathbf{V}_B^H$ and $\mathbf{H}_F = \mathbf{U}_F \Sigma_F \mathbf{V}_F^H$ be the SVD of the backward and forward channels, respectively. The scattering matrix of fully-connected RIS can be decomposed as

$$\mathbf{\Theta} = \mathbf{V}_B \mathbf{X} \mathbf{U}_F^H, \quad (4.6)$$

where $\mathbf{X} \in \mathbb{U}^{N_S \times N_S}$ is a unitary matrix to be designed. The equivalent channel is thus a function of \mathbf{X}

$$\mathbf{H} = \mathbf{H}_B \mathbf{\Theta} \mathbf{H}_F = \mathbf{U}_B \Sigma_B \mathbf{X} \Sigma_F \mathbf{V}_F^H. \quad (4.7)$$

Since $\text{sv}(\mathbf{U}\mathbf{A}\mathbf{V}^H) = \text{sv}(\mathbf{A})$ for unitary \mathbf{U} and \mathbf{V} , we have

$$\begin{aligned} \text{sv}(\mathbf{H}) &= \text{sv}(\mathbf{U}_B \Sigma_B \mathbf{X} \Sigma_F \mathbf{V}_F^H) \\ &= \text{sv}(\Sigma_B \mathbf{X} \Sigma_F) \\ &= \text{sv}(\bar{\mathbf{U}}_B \Sigma_B \bar{\mathbf{V}}_B^H \bar{\mathbf{U}}_F \Sigma_F \bar{\mathbf{V}}_F^H) \\ &= \text{sv}(\mathbf{B}\mathbf{F}), \end{aligned}$$

where $\bar{\mathbf{U}}_{B/F}$ and $\bar{\mathbf{V}}_{B/F}$ are arbitrary unitary matrices.

4.1.5 Proof of Lemma 2

The differential of R w.r.t. $\mathbf{\Theta}_g^*$ is [146]

$$\begin{aligned} \partial R &= \frac{1}{\eta} \text{tr} \left\{ \partial \mathbf{H}^* \cdot \mathbf{Q}^T \mathbf{H}^T \left(\mathbf{I} + \frac{\mathbf{H}^* \mathbf{Q}^T \mathbf{H}^T}{\eta} \right)^{-1} \right\} \\ &= \frac{1}{\eta} \text{tr} \left\{ \mathbf{H}_{B,g}^* \cdot \partial \mathbf{\Theta}_g^* \cdot \mathbf{H}_{F,g}^* \mathbf{Q}^T \mathbf{H}^T \left(\mathbf{I} + \frac{\mathbf{H}^* \mathbf{Q}^T \mathbf{H}^T}{\eta} \right)^{-1} \right\} \\ &= \frac{1}{\eta} \text{tr} \left\{ \mathbf{H}_{F,g}^* \mathbf{Q}^T \mathbf{H}^T \left(\mathbf{I} + \frac{\mathbf{H}^* \mathbf{Q}^T \mathbf{H}^T}{\eta} \right)^{-1} \mathbf{H}_{B,g}^* \cdot \partial \mathbf{\Theta}_g^* \right\}, \end{aligned}$$

and the corresponding complex derivative is (3.26).

4.1.6 Proof of Proposition 4

The differential of (3.28a) w.r.t. Θ_g^* is

$$\begin{aligned}\partial\|\mathbf{H}\|_{\text{F}}^2 &= \text{tr}(\mathbf{H}_{\text{B},g}^* \cdot \partial\Theta_g^* \cdot \mathbf{H}_{\text{F},g}^* (\mathbf{H}_{\text{D}}^{\text{T}} + \mathbf{H}_{\text{F}}^{\text{T}} \Theta^{\text{T}} \mathbf{H}_{\text{B}}^{\text{T}})) \\ &= \text{tr}(\mathbf{H}_{\text{F},g}^* (\mathbf{H}_{\text{D}}^{\text{T}} + \mathbf{H}_{\text{F}}^{\text{T}} \Theta^{\text{T}} \mathbf{H}_{\text{B}}^{\text{T}}) \mathbf{H}_{\text{B},g}^* \cdot \partial\Theta_g^*)\end{aligned}$$

and the corresponding complex derivative is

$$\frac{\partial\|\mathbf{H}\|_{\text{F}}^2}{\partial\Theta_g^*} = \mathbf{H}_{\text{B},g}^{\text{H}} (\mathbf{H}_{\text{D}} + \mathbf{H}_{\text{B}} \Theta \mathbf{H}_{\text{F}}) \mathbf{H}_{\text{F},g}^{\text{H}} = \mathbf{M}_g. \quad (4.8)$$

First, we approximate the quadratic objective (3.28a) by its local Taylor expansion

$$\max_{\Theta} \sum_g 2\Re\{\text{tr}(\Theta_g^{\text{H}} \mathbf{M}_g)\} \quad (4.9a)$$

$$\text{s.t.} \quad \Theta_g^{\text{H}} \Theta_g = \mathbf{I}, \quad \forall g. \quad (4.9b)$$

Let $\mathbf{M}_g = \mathbf{U}_g \Sigma_g \mathbf{V}_g^{\text{H}}$ be the compact SVD of \mathbf{M}_g . We have

$$\Re\{\text{tr}(\Theta_g^{\text{H}} \mathbf{M}_g)\} = \Re\{\text{tr}(\Sigma_g \mathbf{V}_g^{\text{H}} \Theta_g^{\text{H}} \mathbf{U}_g)\} \leq \text{tr}(\Sigma_g). \quad (4.10)$$

The upper bound is tight when $\mathbf{V}_g^{\text{H}} \Theta_g^{\text{H}} \mathbf{U}_g = \mathbf{I}$, which implies the optimal solution of (4.9) is $\tilde{\Theta}_g = \mathbf{U}_g \mathbf{V}_g^{\text{H}}, \forall g$.

Next, we prove that solving (4.9) successively does not decrease (3.28a). Since $\tilde{\Theta}$ optimal for problem (4.9), we have $\sum_g 2\Re\{\text{tr}(\tilde{\Theta}_g^{\text{H}} \mathbf{M}_g)\} \geq \sum_g 2\Re\{\text{tr}(\Theta_g^{\text{H}} \mathbf{M}_g)\}$ which is explicitly expressed by (4.12). On the other hand, expanding $\|\sum_g \mathbf{H}_{\text{B},g} \tilde{\Theta}_g \mathbf{H}_{\text{F},g} - \sum_g \mathbf{H}_{\text{B},g} \Theta_g \mathbf{H}_{\text{F},g}\|_{\text{F}}^2 \geq 0$ gives (4.13). Adding (4.12) and (4.13), we have

$$\begin{aligned}2\Re\left\{\text{tr}(\tilde{\Theta}^{\text{H}} \mathbf{H}_{\text{B}}^{\text{H}} \mathbf{H}_{\text{D}} \mathbf{H}_{\text{F}}^{\text{H}})\right\} + \text{tr}(\mathbf{H}_{\text{F}}^{\text{H}} \tilde{\Theta}^{\text{H}} \mathbf{H}_{\text{B}}^{\text{H}} \mathbf{H}_{\text{B}} \tilde{\Theta} \mathbf{H}_{\text{F}}) \\ \geq 2\Re\left\{\text{tr}(\Theta^{\text{H}} \mathbf{H}_{\text{B}}^{\text{H}} \mathbf{H}_{\text{D}} \mathbf{H}_{\text{F}}^{\text{H}})\right\} + \text{tr}(\mathbf{H}_{\text{F}}^{\text{H}} \Theta^{\text{H}} \mathbf{H}_{\text{B}}^{\text{H}} \mathbf{H}_{\text{B}} \Theta \mathbf{H}_{\text{F}}), \quad (4.11)\end{aligned}$$

which suggests that updating $\tilde{\Theta}$ does not decrease (3.28a).

Finally, we prove that the converging point of (4.9), denoted by $\tilde{\Theta}^?$, is a stationary point of (3.28). The Karush-Kuhn-Tucker (KKT) conditions of (3.28) and (4.9) are equivalent in terms of primal/dual feasibility and complementary slackness, while the stationary conditions

$$2\Re\left\{\sum_g \text{tr}(\tilde{\Theta}_g^H \mathbf{H}_{B,g}^H \mathbf{H}_D \mathbf{H}_{F,g}^H) + \sum_{g_1, g_2} \text{tr}(\tilde{\Theta}_{g_1}^H \mathbf{H}_{B,g_1}^H \mathbf{H}_{B,g_2} \Theta_{g_2} \mathbf{H}_{F,g_2} \mathbf{H}_{F,g_1}^H)\right\} \geq 2\Re\left\{\sum_g \text{tr}(\Theta_g^H \mathbf{H}_{B,g}^H \mathbf{H}_D \mathbf{H}_{F,g}^H) + \sum_{g_1, g_2} \text{tr}(\Theta_{g_1}^H \mathbf{H}_{B,g_1}^H \mathbf{H}_{B,g_2} \Theta_{g_2} \mathbf{H}_{F,g_2} \mathbf{H}_{F,g_1}^H)\right\} \quad (4.12)$$

$$\sum_{g_1, g_2} \text{tr}(\mathbf{H}_{F,g_1}^H \tilde{\Theta}_{g_1}^H \mathbf{H}_{B,g_1}^H \mathbf{H}_{B,g_2} \tilde{\Theta}_{g_2} \mathbf{H}_{F,g_2}) - 2\Re\left\{\sum_{g_1, g_2} \text{tr}(\mathbf{H}_{F,g_1}^H \tilde{\Theta}_{g_1}^H \mathbf{H}_{B,g_1}^H \mathbf{H}_{B,g_2} \Theta_{g_2} \mathbf{H}_{F,g_2})\right\} + \sum_{g_1, g_2} \text{tr}(\mathbf{H}_{F,g_1}^H \Theta_{g_1}^H \mathbf{H}_{B,g_1}^H \mathbf{H}_{B,g_2} \Theta_{g_2} \mathbf{H}_{F,g_2}) \geq 0 \quad (4.13)$$

are respectively, $\forall g$,

$$\mathbf{H}_{B,g}^H (\mathbf{H}_D + \mathbf{H}_B \Theta^* \mathbf{H}_F) \mathbf{H}_{F,g}^H - \Theta_g^* \Lambda_g^H = 0, \quad (4.14)$$

$$\mathbf{M}_g - \Theta_g^* \Lambda_g^H = 0. \quad (4.15)$$

On convergence, (4.15) becomes $\mathbf{H}_{B,g}^H (\mathbf{H}_D + \mathbf{H}_B \Theta^? \mathbf{H}_F) \mathbf{H}_{F,g}^H - \Theta_g^? \Lambda_g^H = 0$ and reduces to (4.14). The proof is thus completed.

References

- [1] Q. Wu and R. Zhang, “Towards smart and reconfigurable environment: Intelligent reflecting surface aided wireless network,” *IEEE Communications Magazine*, vol. 58, pp. 106–112, 1 2020.
- [2] S. Shen, B. Clerckx, and R. Murch, “Modeling and architecture design of reconfigurable intelligent surfaces using scattering parameter network analysis,” *IEEE Transactions on Wireless Communications*, pp. 1–1, Nov. 2021.
- [3] C. E. Shannon, “A mathematical theory of communication,” *Bell System Technical Journal*, vol. 27, pp. 379–423, Jul 1948.
- [4] F. Tariq, M. R. A. Khandaker, K.-K. Wong, M. A. Imran, M. Bennis, and M. Debbah, “A speculative study on 6g,” *IEEE Wireless Communications*, vol. 27, pp. 118–125, 8 2020.
- [5] D. Georgiev, “Internet of things statistics, facts & predictions [2024’s update],” <https://review42.com/resources/internet-of-things-stats/>, accessed: 2024-03-13.
- [6] M. Shafi, A. F. Molisch, P. J. Smith, T. Haustein, P. Zhu, P. D. Silva, F. Tufvesson, A. Benjebbour, and G. Wunder, “5g: A tutorial overview of standards, trials, challenges, deployment, and practice,” *IEEE Journal on Selected Areas in Communications*, vol. 35, pp. 1201–1221, 6 2017.
- [7] H. Tataria, M. Shafi, A. F. Molisch, M. Dohler, H. Sjoland, and F. Tufvesson, “6g wireless systems: Vision, requirements, challenges, insights, and opportunities,” *Proceedings of the IEEE*, vol. 109, pp. 1166–1199, 7 2021.
- [8] M. Alsabah, M. A. Naser, B. M. Mahmmod, S. H. Abdulhussain, M. R. Eissa, A. Al-Baidhani, N. K. Noordin, S. M. Sait, K. A. Al-Utaibi, and F. Hashim, “6g wireless communications networks: A comprehensive survey,” *IEEE Access*, vol. 9, pp. 148 191–148 243, 2021.
- [9] W. Jiang, B. Han, M. A. Habibi, and H. D. Schotten, “The road towards 6g: A comprehensive survey,” *IEEE Open Journal of the Communications Society*, vol. 2, pp. 334–366, 2021.
- [10] L. Dai, B. Wang, M. Wang, X. Yang, J. Tan, S. Bi, S. Xu, F. Yang, Z. Chen, M. D. Renzo, C.-B. Chae, and L. Hanzo, “Reconfigurable intelligent surface-based wireless communications: Antenna design, prototyping, and experimental results,” *IEEE Access*, vol. 8, pp. 45 913–45 923, 2020.

- [11] P. Nayeri, F. Yang, and A. Z. Elsherbeni, *Reflectarray Antennas: Theory, Designs, and Applications*. Wiley, 2 2018.
- [12] R. Anwar, L. Mao, and H. Ning, “Frequency selective surfaces: A review,” *Applied Sciences*, vol. 8, no. 9, p. 1689, Sep. 2018.
- [13] Q. Wu, X. Zhou, and R. Schober, “IRS-assisted wireless powered NOMA: Do we really need different phase shifts in DL and UL?” *IEEE Wireless Communications Letters*, vol. 10, pp. 1493–1497, Jul 2021.
- [14] Q. Wu and R. Zhang, “Intelligent reflecting surface enhanced wireless network via joint active and passive beamforming,” *IEEE Transactions on Wireless Communications*, vol. 18, pp. 5394–5409, Nov 2019.
- [15] T. Jiang and W. Yu, “Interference nulling using reconfigurable intelligent surface,” *IEEE Journal on Selected Areas in Communications*, vol. 40, pp. 1392–1406, 5 2022.
- [16] G. Ghatak, V. Malik, S. S. Kalamkar, and A. K. Gupta, “Where to deploy reconfigurable intelligent surfaces in the presence of blockages?” vol. 2021-September. IEEE, 9 2021, pp. 1419–1424.
- [17] S. Zeng, H. Zhang, B. Di, Z. Han, and L. Song, “Reconfigurable intelligent surface (ris) assisted wireless coverage extension: Ris orientation and location optimization,” *IEEE Communications Letters*, vol. 25, pp. 269–273, 1 2021.
- [18] A. Almohamad, A. M. Tahir, A. Al-Kababji, H. M. Furqan, T. Khattab, M. O. Hasna, and H. Arslan, “Smart and secure wireless communications via reflecting intelligent surfaces: A short survey,” *IEEE Open Journal of the Communications Society*, vol. 1, pp. 1442–1456, 2020.
- [19] J. Ye, S. Guo, S. Dang, B. Shihada, and M.-S. Alouini, “On the capacity of reconfigurable intelligent surface assisted mimo symbiotic communications,” *IEEE Transactions on Wireless Communications*, vol. 21, pp. 1943–1959, 3 2022.
- [20] E. Basar, “Reconfigurable intelligent surfaces for doppler effect and multipath fading mitigation,” *Frontiers in Communications and Networks*, vol. 2, 5 2021.
- [21] E. Arslan, I. Yildirim, F. Kilinc, and E. Basar, “Over-the-air equalization with reconfigurable intelligent surfaces,” *IET Communications*, vol. 16, pp. 1486–1497, 8 2022.
- [22] O. Ozdogan, E. Bjornson, and E. G. Larsson, “Using intelligent reflecting surfaces for rank improvement in mimo communications.” IEEE, 5 2020, pp. 9160–9164.
- [23] Y. Yang, B. Zheng, S. Zhang, and R. Zhang, “Intelligent reflecting surface meets ofdm: Protocol design and rate maximization,” *IEEE Transactions on Communications*, vol. 68, pp. 4522–4535, 7 2020.
- [24] G. Chen and Q. Wu, “Fundamental limits of intelligent reflecting surface aided multiuser broadcast channel,” *IEEE Transactions on Communications*, vol. 71, pp. 5904–5919, 10 2023.

- [25] R. Liu, Q. Wu, M. D. Renzo, and Y. Yuan, "A path to smart radio environments: An industrial viewpoint on reconfigurable intelligent surfaces," *IEEE Wireless Communications*, vol. 29, pp. 202–208, 2 2022.
- [26] R. Alliance, "Reconfigurable intelligent surface technology white paper," 2023.
- [27] ITU-R, "Future technology trends of terrestrial international mobile telecommunications systems towards 2030 and beyond," Report ITU-R M.2516-0, 2022.
- [28] Y. Zhao, B. Clerckx, and Z. Feng, "IRS-aided SWIPT: Joint waveform, active and passive beamforming design under nonlinear harvester model," *IEEE Transactions on Communications*, vol. 70, pp. 1345–1359, 2022.
- [29] Y. Zhao and B. Clerckx, "Riscatter: Unifying backscatter communication and reconfigurable intelligent surface," 12 2022.
- [30] —, *RIS in Wireless Information and Power Transfer*. John Wiley & Sons, Ltd, 2023, pp. 271–295.
- [31] Y. Zhao, H. Li, M. Franceschetti, and B. Clerckx, "Channel shaping using reconfigurable intelligent surfaces: From diagonal to beyond," *To be submitted to IEEE Transactions on Wireless Communications*.
- [32] V. G. Veselago, "The electrodynamics of substances with negative ϵ and μ ," *Soviet Physics Uspekhi*, vol. 10, pp. 509–514, 4 1968.
- [33] J. Pendry, A. Holden, D. Robbins, and W. Stewart, "Magnetism from conductors and enhanced nonlinear phenomena," *IEEE Transactions on Microwave Theory and Techniques*, vol. 47, pp. 2075–2084, 1999.
- [34] N. Yu, P. Genevet, M. A. Kats, F. Aieta, J.-P. Tetienne, F. Capasso, and Z. Gaburro, "Light propagation with phase discontinuities: Generalized laws of reflection and refraction," *Science*, vol. 334, pp. 333–337, 10 2011.
- [35] J. Pendry, "Negative refraction," *Contemporary Physics*, vol. 45, pp. 191–202, 5 2004.
- [36] T. J. Cui, M. Q. Qi, X. Wan, J. Zhao, and Q. Cheng, "Coding metamaterials, digital metamaterials and programmable metamaterials," *Light: Science & Applications*, vol. 3, no. 10, pp. e218–e218, Oct. 2014.
- [37] Q. Ma, G. D. Bai, H. B. Jing, C. Yang, L. Li, and T. J. Cui, "Smart metasurface with self-adaptively reprogrammable functions," *Light: Science & Applications*, vol. 8, p. 98, 10 2019.
- [38] W. J. Padilla, D. N. Basov, and D. R. Smith, "Negative refractive index metamaterials," *Materials Today*, vol. 9, pp. 28–35, 7 2006.
- [39] M. Poulakis, "6g's metamaterials solution: There's plenty of bandwidth available if we use reconfigurable intelligent surfaces," *IEEE Spectrum*, vol. 59, pp. 40–45, 11 2022.
- [40] Y. C. Liang, Q. Zhang, J. Wang, R. Long, H. Zhou, and G. Yang, "Backscatter communication assisted by reconfigurable intelligent surfaces," *Proceedings of the IEEE*, 2022.

- [41] R. Hansen, "Relationships between antennas as scatterers and as radiators," *Proceedings of the IEEE*, vol. 77, pp. 659–662, May 1989.
- [42] S. J. Thomas and M. S. Reynolds, "A 96 mbit/sec, 15.5 pj/bit 16-qam modulator for uhf backscatter communication." IEEE, Apr 2012, pp. 185–190.
- [43] Y.-C. Liang, Q. Zhang, E. G. Larsson, and G. Y. Li, "Symbiotic radio: Cognitive backscattering communications for future wireless networks," *IEEE Transactions on Cognitive Communications and Networking*, vol. 6, pp. 1242–1255, Dec 2020.
- [44] C. Boyer and S. Roy, "Backscatter communication and RFID: Coding, energy, and MIMO analysis," *IEEE Transactions on Communications*, vol. 62, pp. 770–785, Mar 2014.
- [45] O. Ozdogan, E. Bjornson, and E. G. Larsson, "Intelligent reflecting surfaces: Physics, propagation, and pathloss modeling," *IEEE Wireless Communications Letters*, vol. 9, no. 5, pp. 581–585, May 2020.
- [46] M. Najafi, V. Jamali, R. Schober, and H. V. Poor, "Physics-based modeling and scalable optimization of large intelligent reflecting surfaces," *IEEE Transactions on Communications*, vol. 69, pp. 2673–2691, 4 2021.
- [47] S. Abeywickrama, R. Zhang, and C. Yuen, "Intelligent reflecting surface: Practical phase shift model and beamforming optimization," in *ICC 2020 - 2020 IEEE International Conference on Communications (ICC)*. IEEE, Jun. 2020, pp. 1–6.
- [48] Q. Wu and R. Zhang, "Intelligent reflecting surface enhanced wireless network: Joint active and passive beamforming design," vol. 18. IEEE, Dec 2018, pp. 1–6.
- [49] M. T. Ivrlac and J. A. Nossek, "Toward a circuit theory of communication," *IEEE Transactions on Circuits and Systems I: Regular Papers*, vol. 57, pp. 1663–1683, 7 2010.
- [50] H.-R. Ahn, *Asymmetric Passive Components in Microwave Integrated Circuits*. Wiley, 2006.
- [51] M. Nerini, S. Shen, H. Li, and B. Clerckx, "Beyond diagonal reconfigurable intelligent surfaces utilizing graph theory: Modeling, architecture design, and optimization," 5 2023.
- [52] X. Mu, Y. Liu, L. Guo, J. Lin, and R. Schober, "Simultaneously transmitting and reflecting (star) ris aided wireless communications," *IEEE Transactions on Wireless Communications*, vol. 21, pp. 3083–3098, 5 2022.
- [53] Y. Liu, X. Mu, J. Xu, R. Schober, Y. Hao, H. V. Poor, and L. Hanzo, "Star: Simultaneous transmission and reflection for 360° coverage by intelligent surfaces," *IEEE Wireless Communications*, vol. 28, pp. 102–109, 12 2021.
- [54] H. Li, S. Shen, and B. Clerckx, "Beyond diagonal reconfigurable intelligent surfaces: A multi-sector mode enabling highly directional full-space wireless coverage," *IEEE Journal on Selected Areas in Communications*, vol. 41, pp. 2446–2460, 8 2023.

- [55] J. Koomey, S. Berard, M. Sanchez, and H. Wong, "Implications of historical trends in the electrical efficiency of computing," *IEEE Annals of the History of Computing*, vol. 33, pp. 46–54, 3 2011.
- [56] J. Huang, Y. Zhou, Z. Ning, and H. Gharavi, "Wireless power transfer and energy harvesting: Current status and future prospects," *IEEE Wireless Communications*, vol. 26, pp. 163–169, 8 2019.
- [57] X. Hao, H. Zhang, Z. Shen, Z. Liu, L. Zhang, H. Jiang, J. Liu, and H. Liao, "A 43.2 μ W 2.4 ghz 64-qam pseudo-backscatter modulator based on integrated directional coupler." *IEEE*, 5 2018, pp. 1–5.
- [58] R. Correia and N. B. Carvalho, "Ultrafast backscatter modulator with low-power consumption and wireless power transmission capabilities," *IEEE Microwave and Wireless Components Letters*, vol. 27, pp. 1152–1154, 12 2017.
- [59] J. Zhou, P. Zhang, J. Han, L. Li, and Y. Huang, "Metamaterials and metasurfaces for wireless power transfer and energy harvesting," *Proceedings of the IEEE*, vol. 110, pp. 31–55, 1 2022.
- [60] J. Joung, C. K. Ho, K. Adachi, and S. Sun, "A survey on power-amplifier-centric techniques for spectrum- and energy-efficient wireless communications," *IEEE Communications Surveys & Tutorials*, vol. 17, pp. 315–333, 1 2015.
- [61] A. Alizadeh, S. Hassanzadehyamchi, A. Medi, and S. Kiaei, "An x-band class-j power amplifier with active load modulation to boost drain efficiency," *IEEE Transactions on Circuits and Systems I: Regular Papers*, vol. 67, pp. 3364–3377, 10 2020.
- [62] N. M. L. Tan, T. Abe, and H. Akagi, "Design and performance of a bidirectional isolated dc-dc converter for a battery energy storage system," *IEEE Transactions on Power Electronics*, vol. 27, pp. 1237–1248, 3 2012.
- [63] B. Clerckx and E. Bayguzina, "Waveform design for wireless power transfer," *IEEE Transactions on Signal Processing*, vol. 64, no. 23, pp. 6313–6328, Dec. 2016.
- [64] C. R. Valenta and G. D. Durgin, "Harvesting wireless power: Survey of energy-harvester conversion efficiency in far-field, wireless power transfer systems," *IEEE Microwave Magazine*, vol. 15, pp. 108–120, 6 2014.
- [65] S. A. Rotenberg, S. K. Podilchak, P. D. H. Re, C. Mateo-Segura, G. Goussetis, and J. Lee, "Efficient rectifier for wireless power transmission systems," *IEEE Transactions on Microwave Theory and Techniques*, vol. 68, pp. 1921–1932, 5 2020.
- [66] E. Boshkovska, D. W. K. Ng, N. Zlatanov, and R. Schober, "Practical non-linear energy harvesting model and resource allocation for swipt systems," *IEEE Communications Letters*, vol. 19, pp. 2082–2085, 12 2015.
- [67] Y. Zeng, B. Clerckx, and R. Zhang, "Communications and signals design for wireless power transmission," *IEEE Transactions on Communications*, vol. 65, pp. 2264–2290, 5 2017.

- [68] M. D. Prete, A. Costanzo, M. Magno, D. Masotti, and L. Benini, "Optimum excitations for a dual-band microwatt wake-up radio," *IEEE Transactions on Microwave Theory and Techniques*, vol. 64, pp. 4731–4739, 12 2016.
- [69] Y. Huang and B. Clerckx, "Large-scale multiantenna multisine wireless power transfer," *IEEE Transactions on Signal Processing*, vol. 65, pp. 5812–5827, 11 2017.
- [70] S. Shen and B. Clerckx, "Beamforming optimization for mimo wireless power transfer with nonlinear energy harvesting: Rf combining versus dc combining," *IEEE Transactions on Wireless Communications*, vol. 20, pp. 199–213, 1 2021.
- [71] L. R. Varshney, "Transporting information and energy simultaneously," in *2008 IEEE International Symposium on Information Theory*. IEEE, Jul. 2008, pp. 1612–1616.
- [72] B. Clerckx, "Wireless information and power transfer: Nonlinearity, waveform design, and rate-energy tradeoff," *IEEE Transactions on Signal Processing*, vol. 66, no. 4, pp. 847–862, Feb. 2018.
- [73] B. Clerckx, R. Zhang, R. Schober, D. W. K. Ng, D. I. Kim, and H. V. Poor, "Fundamentals of wireless information and power transfer: From RF energy harvester models to signal and system designs," *IEEE Journal on Selected Areas in Communications*, vol. 37, no. 1, pp. 4–33, Jan. 2019.
- [74] T. M. Cover and J. A. Thomas, *Elements of Information Theory*. Wiley, 9 2005.
- [75] M. Trotter, J. Griffin, and G. Durgin, "Power-optimized waveforms for improving the range and reliability of RFID systems," in *2009 IEEE International Conference on RFID*. IEEE, Apr. 2009, pp. 80–87.
- [76] Q. Wu, X. Guan, and R. Zhang, "Intelligent reflecting surface-aided wireless energy and information transmission: An overview," *Proceedings of the IEEE*, vol. 110, pp. 150–170, 1 2022.
- [77] X. Lu, P. Wang, D. Niyato, D. I. Kim, and Z. Han, "Wireless networks with rf energy harvesting: A contemporary survey," *IEEE Communications Surveys & Tutorials*, vol. 17, pp. 757–789, 2015.
- [78] B. Clerckx, J. Kim, K. W. Choi, and D. I. Kim, "Foundations of wireless information and power transfer: Theory, prototypes, and experiments," *Proceedings of the IEEE*, vol. 110, pp. 8–30, 1 2022.
- [79] J. Kim and B. Clerckx, "Wireless information and power transfer for IoT: Pulse position modulation, integrated receiver, and experimental validation," *IEEE Internet of Things Journal*, vol. 9, pp. 12 378–12 394, Jul 2022.
- [80] H. Stockman, "Communication by means of reflected power," *Proceedings of the IRE*, vol. 36, pp. 1196–1204, 10 1948.
- [81] J. Landt, "The history of RFID," *IEEE Potentials*, vol. 24, pp. 8–11, Oct 2005.
- [82] Q. H. Abbasi, H. T. Abbas, A. Alomainy, and M. A. Imran, *Backscattering and RF Sensing for Future Wireless Communication*. Wiley, 6 2021.

- [83] G. Yang, C. K. Ho, and Y. L. Guan, "Multi-antenna wireless energy transfer for backscatter communication systems," *IEEE Journal on Selected Areas in Communications*, vol. 33, pp. 2974–2987, Dec 2015.
- [84] C. Chen, G. Wang, H. Guan, Y.-C. Liang, and C. Tellambura, "Transceiver design and signal detection in backscatter communication systems with multiple-antenna tags," *IEEE Transactions on Wireless Communications*, vol. 19, pp. 3273–3288, 5 2020.
- [85] E. Goudeli, C. Psomas, and I. Krikidis, "Spatial-modulation-based techniques for backscatter communication systems," *IEEE Internet of Things Journal*, vol. 7, pp. 10 623–10 634, 10 2020.
- [86] W. Liu, S. Shen, D. H. K. Tsang, and R. Murch, "Enhancing ambient backscatter communication utilizing coherent and non-coherent space-time codes," *IEEE Transactions on Wireless Communications*, vol. 20, pp. 6884–6897, 10 2021.
- [87] C. He, S. Chen, H. Luan, X. Chen, and Z. J. Wang, "Monostatic mimo backscatter communications," *IEEE Journal on Selected Areas in Communications*, vol. 38, pp. 1896–1909, 8 2020.
- [88] X. Wang, H. Yigitler, R. Duan, E. Y. Menta, and R. Jantti, "Coherent multi-antenna receiver for bpsk-modulated ambient backscatter tags," *IEEE Internet of Things Journal*, vol. 4662, pp. 1–1, 2021.
- [89] J. K. Devineni and H. S. Dhillon, "Non-coherent detection and bit error rate for an ambient backscatter link in time-selective fading," *IEEE Transactions on Communications*, vol. 69, pp. 602–618, 1 2021.
- [90] S. J. Thomas, E. Wheeler, J. Teizer, and M. S. Reynolds, "Quadrature amplitude modulated backscatter in passive and semipassive UHF RFID systems," *IEEE Transactions on Microwave Theory and Techniques*, vol. 60, pp. 1175–1182, Apr 2012.
- [91] P. Zhang, D. Bharadia, K. Joshi, and S. Katti, "Hitchhike: Practical backscatter using commodity wifi." *ACM*, 11 2016, pp. 259–271.
- [92] V. Iyer, V. Talla, B. Kellogg, S. Gollakota, and J. Smith, "Inter-technology backscatter: Towards internet connectivity for implanted devices vikram." *ACM*, 8 2016, pp. 356–369.
- [93] B. Kellogg, V. Talla, J. R. Smith, and S. Gollakot, "Passive wi-fi: Bringing low power to wi-fi transmissions," *GetMobile: Mobile Computing and Communications*, vol. 20, pp. 38–41, 1 2017.
- [94] J. F. Ensworth and M. S. Reynolds, "Ble-backscatter: Ultralow-power iot nodes compatible with bluetooth 4.0 low energy (ble) smartphones and tablets," *IEEE Transactions on Microwave Theory and Techniques*, vol. 65, pp. 3360–3368, 9 2017.
- [95] V. Talla, M. Hesar, B. Kellogg, A. Najafi, J. R. Smith, and S. Gollakota, "Lora backscatter: Enabling the vision of ubiquitous connectivity," *Proceedings of the ACM on Interactive, Mobile, Wearable and Ubiquitous Technologies*, vol. 1, pp. 1–24, 9 2017.

- [96] D. T. Hoang, D. Niyato, D. I. Kim, T. Kim, N. V. Huynh, and S. Gong, *Ambient Backscatter Communication Networks*. Cambridge University Press, 2020.
- [97] V. Liu, A. Parks, V. Talla, S. Gollakota, D. Wetherall, and J. R. Smith, “Ambient backscatter: Wireless communication out of thin air,” *ACM SIGCOMM Computer Communication Review*, vol. 43, pp. 39–50, Sep 2013.
- [98] H. Guo, Y.-C. Liang, R. Long, and Q. Zhang, “Cooperative ambient backscatter system: A symbiotic radio paradigm for passive IoT,” *IEEE Wireless Communications Letters*, vol. 8, pp. 1191–1194, Aug 2019.
- [99] E. Basar, M. D. Renzo, J. D. Rosny, M. Debbah, M.-S. Alouini, and R. Zhang, “Wireless communications through reconfigurable intelligent surfaces,” *IEEE Access*, vol. 7, pp. 116 753–116 773, 2019.
- [100] Q. Wu and R. Zhang, “Beamforming optimization for wireless network aided by intelligent reflecting surface with discrete phase shifts,” *IEEE Transactions on Communications*, vol. 68, no. 3, pp. 1838–1851, Mar. 2020.
- [101] Y. Yang, S. Zhang, and R. Zhang, “IRS-enhanced OFDMA: Joint resource allocation and passive beamforming optimization,” *IEEE Wireless Communications Letters*, vol. 9, pp. 760–764, Jun 2020.
- [102] B. Zheng, C. You, and R. Zhang, “Double-irs assisted multi-user mimo: Cooperative passive beamforming design,” *IEEE Transactions on Wireless Communications*, vol. 20, pp. 4513–4526, 7 2021.
- [103] X. Jia, J. Zhao, X. Zhou, and D. Niyato, “Intelligent reflecting surface-aided backscatter communications,” vol. 2020-Janua. IEEE, 12 2020, pp. 1–6.
- [104] R. Liu, M. Li, Y. Liu, Q. Wu, and Q. Liu, “Joint transmit waveform and passive beamforming design for ris-aided dfrc systems,” *IEEE Journal of Selected Topics in Signal Processing*, pp. 1–1, 5 2022.
- [105] M. Hua, Q. Wu, C. He, S. Ma, and W. Chen, “Joint active and passive beamforming design for irs-aided radar-communication,” *IEEE Transactions on Wireless Communications*, vol. 22, pp. 2278–2294, 4 2023.
- [106] Q. Wu, X. Zhou, W. Chen, J. Li, and X. Zhang, “IRS-aided WPCNs: A new optimization framework for dynamic IRS beamforming,” *IEEE Transactions on Wireless Communications*, pp. 1–1, Dec 2021.
- [107] Z. Feng, B. Clerckx, and Y. Zhao, “Waveform and beamforming design for intelligent reflecting surface aided wireless power transfer: Single-user and multi-user solutions,” *IEEE Transactions on Wireless Communications*, 2022.
- [108] R. Karasik, O. Simeone, M. D. Renzo, and S. S. Shitz, “Beyond max-SNR: Joint encoding for reconfigurable intelligent surfaces,” vol. 2020-June. IEEE, Jun 2020, pp. 2965–2970.

- [109] E. Basar, “Reconfigurable intelligent surface-based index modulation: A new beyond MIMO paradigm for 6G,” *IEEE Transactions on Communications*, vol. 68, pp. 3187–3196, May 2020.
- [110] W. Tang, J. Y. Dai, M. Chen, X. Li, Q. Cheng, S. Jin, K.-K. Wong, and T. J. Cui, “Programmable metasurface-based RF chain-free 8PSK wireless transmitter,” *Electronics Letters*, vol. 55, pp. 417–420, Apr 2019.
- [111] J. Y. Dai, W. Tang, L. X. Yang, X. Li, M. Z. Chen, J. C. Ke, Q. Cheng, S. Jin, and T. J. Cui, “Realization of multi-modulation schemes for wireless communication by time-domain digital coding metasurface,” *IEEE Transactions on Antennas and Propagation*, vol. 68, pp. 1618–1627, Mar 2020.
- [112] H. Li, S. Shen, and B. Clerckx, “Beyond diagonal reconfigurable intelligent surfaces: From transmitting and reflecting modes to single-, group-, and fully-connected architectures,” *IEEE Transactions on Wireless Communications*, vol. 22, pp. 2311–2324, 4 2023.
- [113] M. Nerini, S. Shen, and B. Clerckx, “Closed-form global optimization of beyond diagonal reconfigurable intelligent surfaces,” *IEEE Transactions on Wireless Communications*, pp. 1–1, 2023.
- [114] I. Santamaria, M. Soleymani, E. Jorswieck, and J. Gutiérrez, “Snr maximization in beyond diagonal ris-assisted single and multiple antenna links,” *IEEE Signal Processing Letters*, vol. 30, pp. 923–926, 2023.
- [115] T. Fang and Y. Mao, “A low-complexity beamforming design for beyond-diagonal ris aided multi-user networks,” *IEEE Communications Letters*, pp. 1–1, 7 2023.
- [116] Y. Zhou, Y. Liu, H. Li, Q. Wu, S. Shen, and B. Clerckx, “Optimizing power consumption, energy efficiency and sum-rate using beyond diagonal ris — a unified approach,” *IEEE Transactions on Wireless Communications*, pp. 1–1, 2023.
- [117] H. Li, S. Shen, and B. Clerckx, “A dynamic grouping strategy for beyond diagonal reconfigurable intelligent surfaces with hybrid transmitting and reflecting mode,” *IEEE Transactions on Vehicular Technology*, 12 2023.
- [118] G. Bartoli, A. Abrardo, N. Decarli, D. Dardari, and M. D. Renzo, “Spatial multiplexing in near field mimo channels with reconfigurable intelligent surfaces,” *IET Signal Processing*, vol. 17, 3 2023.
- [119] H. Li, Y. Zhang, and B. Clerckx, “Channel estimation for beyond diagonal reconfigurable intelligent surfaces with group-connected architectures,” 7 2023.
- [120] H. Li, S. Shen, M. Nerini, M. D. Renzo, and B. Clerckx, “Beyond diagonal reconfigurable intelligent surfaces with mutual coupling: Modeling and optimization,” 10 2023.
- [121] H. Li, S. Shen, M. Nerini, and B. Clerckx, “Reconfigurable intelligent surfaces 2.0: Beyond diagonal phase shift matrices,” 1 2023.

- [122] M. A. ElMossallamy, H. Zhang, R. Sultan, K. G. Seddik, L. Song, G. Y. Li, and Z. Han, "On spatial multiplexing using reconfigurable intelligent surfaces," *IEEE Wireless Communications Letters*, vol. 10, pp. 226–230, 2 2021.
- [123] S. Meng, W. Tang, W. Chen, J. Lan, Q. Y. Zhou, Y. Han, X. Li, and S. Jin, "Rank optimization for mimo channel with ris: Simulation and measurement," 7 2023.
- [124] Y. Zheng, T. Lin, and Y. Zhu, "Passive beamforming for irs-assisted mu-mimo systems with one-bit adcs: An ser minimization design approach," *IEEE Communications Letters*, vol. 26, pp. 1101–1105, 5 2022.
- [125] W. Huang, B. Lei, S. He, C. Kai, and C. Li, "Condition number improvement of irs-aided near-field mimo channels," *IEEE*, 5 2023, pp. 1210–1215.
- [126] A. H. Bafghi, V. Jamali, M. Nasiri-Kenari, and R. Schober, "Degrees of freedom of the k-user interference channel assisted by active and passive irss," *IEEE Transactions on Communications*, vol. 70, pp. 3063–3080, 5 2022.
- [127] S. Zheng, B. Lv, T. Zhang, Y. Xu, G. Chen, R. Wang, and P. C. Ching, "On dof of active ris-assisted mimo interference channel with arbitrary antenna configurations: When will ris help?" *IEEE Transactions on Vehicular Technology*, 12 2023.
- [128] S. H. Chae and K. Lee, "Cooperative communication for the rank-deficient mimo interference channel with a reconfigurable intelligent surface," *IEEE Transactions on Wireless Communications*, vol. 22, pp. 2099–2112, 3 2023.
- [129] I. Santamaria, M. Soleymani, E. Jorswieck, and J. Gutiérrez, "Interference leakage minimization in ris-assisted mimo interference channels," vol. 39. *IEEE*, 6 2023, pp. 1–5.
- [130] T. E. Abrudan, J. Eriksson, and V. Koivunen, "Steepest descent algorithms for optimization under unitary matrix constraint," *IEEE Transactions on Signal Processing*, vol. 56, pp. 1134–1147, 3 2008.
- [131] T. Abrudan, J. Eriksson, and V. Koivunen, "Conjugate gradient algorithm for optimization under unitary matrix constraint," *Signal Processing*, vol. 89, pp. 1704–1714, 9 2009.
- [132] P.-A. Absil, R. Mahony, and R. Sepulchre, *Optimization Algorithms on Matrix Manifolds*. Princeton University Press, 2009.
- [133] C. Pan, G. Zhou, K. Zhi, S. Hong, T. Wu, Y. Pan, H. Ren, M. D. Renzo, A. L. Swindlehurst, R. Zhang, and A. Y. Zhang, "An overview of signal processing techniques for ris/irs-aided wireless systems," *IEEE Journal of Selected Topics in Signal Processing*, vol. 16, pp. 883–917, 8 2022.
- [134] A. Edelman, T. A. Arias, and S. T. Smith, "The geometry of algorithms with orthogonality constraints," *SIAM Journal on Matrix Analysis and Applications*, vol. 20, pp. 303–353, 1 1998.

- [135] E. Polak and G. Ribiere, “Note sur la convergence de méthodes de directions conjuguées,” *Revue française d’informatique et de recherche opérationnelle. Série rouge*, vol. 3, pp. 35–43, 1969.
- [136] L. Armijo, “Minimization of functions having lipschitz continuous first partial derivatives,” *Pacific Journal of Mathematics*, vol. 16, pp. 1–3, 1 1966.
- [137] D. Semmler, M. Joham, and W. Utschick, “High snr analysis of ris-aided mimo broadcast channels,” in *2023 IEEE 24th International Workshop on Signal Processing Advances in Wireless Communications (SPAWC)*. IEEE, 9 2023, pp. 221–225.
- [138] W. Fulton, “Eigenvalues, invariant factors, highest weights, and schubert calculus,” *Bulletin of the American Mathematical Society*, vol. 37, pp. 209–249, 4 2000.
- [139] B. Clerckx and C. Oestges, *MIMO Wireless Networks: Channels, Techniques and Standards for Multi-Antenna, Multi-User and Multi-Cell Systems*. Elsevier Science, 2013.
- [140] J. C. Gower and G. B. Dijksterhuis, *Procrustes Problems*. OUP Oxford, 2004.
- [141] T. Bell, “Global positioning system-based attitude determination and the orthogonal procrustes problem,” *Journal of Guidance, Control, and Dynamics*, vol. 26, pp. 820–822, 9 2003.
- [142] G. H. Golub and C. F. Van Loan, *Matrix Computations*. Baltimore, MD, USA: Johns Hopkins University Press, 2013.
- [143] F. Nie, R. Zhang, and X. Li, “A generalized power iteration method for solving quadratic problem on the stiefel manifold,” *Science China Information Sciences*, vol. 60, p. 112101, 11 2017.
- [144] K. Gomadam, V. R. Cadambe, and S. A. Jafar, “A distributed numerical approach to interference alignment and applications to wireless interference networks,” *IEEE Transactions on Information Theory*, vol. 57, pp. 3309–3322, 6 2011.
- [145] F. Negro, S. P. Shenoy, I. Ghauri, and D. T. Slock, “Weighted sum rate maximization in the mimo interference channel.” IEEE, 9 2010, pp. 684–689.
- [146] A. Hjørungnes and D. Gesbert, “Complex-valued matrix differentiation: Techniques and key results,” *IEEE Transactions on Signal Processing*, vol. 55, pp. 2740–2746, 6 2007.